First superheavy element experiments at the GSI recoil separator TASCA: The production and decay of element 114 in the ^{244}Pu(^{48}Ca,3-4n) reaction

J. M. Gates *et al.*

Phys. Rev. C **83**, 054618 — Published 27 May 2011

DOI: 10.1103/PhysRevC.83.054618

First superheavy element experiments at TASCA: the production and decay of element 114 in the ^{244}Pu(^{48}Ca,3-4*n*) reaction

J. M. Gates,[1,2,3,*] Ch.E. Düllmann,[1,4,5] M. Schädel,[1] A. Yakushev,[2] A. Türler,[2,#] K. Eberhardt,[4] J.V. Kratz,[4] D. Ackermann,[1] L.-L. Andersson,[6] M. Block,[1] W. Brüchle,[1] J. Dvorak,[3] H.G. Essel,[1] P.A. Ellison,[3,7] J. Even,[4] U. Forsberg,[8] J. Gellanki,[8] A. Gorshkov,[2] R. Graeger,[2] K.E. Gregorich,[3] W. Hartmann,[1] R.-D. Herzberg,[6] F.P. Heßberger,[1] D. Hild,[4] A. Hübner,[1] E. Jäger,[1] J. Khuyagbaatar,[1] B. Kindler,[1] J. Krier,[1] N. Kurz,[1] S. Lahiri,[9] D. Liebe,[4] B. Lommel,[1] M. Maiti,[9] H. Nitsche,[3,7] J.P. Omtvedt,[10] E. Parr,[6] D. Rudolph,[8] J. Runke,[4] H. Schaffner,[1] B. Schausten,[1] E. Schimpf,[1] A. Semchenkov,[10] J. Steiner,[1] P. Thörle-Pospiech,[4] J. Uusitalo,[11] M. Wegrzecki,[12] N. Wiehl[4]

[1]*GSI Helmholtzzentrum für Schwerionenforschung GmbH, 64291 DARMSTADT, GERMANY*

[2]*Technische Universität München, 85748 GARCHING, GERMANY*

[3]*Lawrence Berkeley National Laboratory, BERKELEY, California 94720-8169, USA*

[4]*Johannes Gutenberg-Universität Mainz, 55099 MAINZ, GERMANY*

[5]*Helmholtz Institute Mainz, 55099 MAINZ, GERMANY*

[6]*University of Liverpool, LIVERPOOL, L69 7ZE, UK*

[7]*University of California, BERKELEY, California 94720-1460, USA*

[8]*Lund University, 22100 LUND, SWEDEN*

[9]*Saha Institute of Nuclear Physics, KOLKATA-700064, INDIA*

[10]*University of Oslo, 0315 OSLO, NORWAY*

[11]*University of Jyväskylä, 40014 JYVÄSKYLÄ, FINLAND*

[12]*Institute of Electron Technology, 02-668 WARSAW, POLAND*

[*]Electronic address: jmgates@lbl.gov

[#]Present address: Paul Scherrer Institute and University of Bern, 5232 Villigen, Switzerland.

(Received)

Abstract

Experiments with the new recoil separator, TASCA, at the GSI were performed using beams of ^{48}Ca to irradiate targets of $^{206-208}$Pb leading to the production of $^{252-254}$No isotopes. These studies allowed for evaluation of the performance of TASCA when coupled to a new detector and electronics system. Following these studies, the isotopes of element 114 (^{288,289}114) were produced in irradiations of ^{244}Pu targets with ^{48}Ca beams at compound nucleus excitation energies around 41.7 and 37.5 MeV, demonstrating TASCA's ability to perform experiments with picobarn-level cross sections. A total of fifteen decay chains were observed and assigned to the decay of ^{288,289}114. A new α-decay branch in ^{281}Ds was observed, leading to the new nucleus ^{277}Hs.

PACS numbers: 25.70.Jj, 27.90.+b, 25.70.-z

I. INTRODUCTION

The TransActinide Separator and Chemistry Apparatus (TASCA) is a recently-installed recoil-separator at the GSI Helmholtzzentrum für Schwerionenforschung (GSI) in Darmstadt, Germany [1]. It was optimized for the study of neutron-rich transactinide (TAN, $Z \geq 104$) elements produced in hot fusion reactions between highly-intense ion beams and actinide targets. Due to production rates on the order of nano- (Z=104) to femtobarns (Z=113 [2]), TASCA was designed to i) separate the TAN of interest from the beam and plethora of unwanted reaction products, and ii) maximize the transmission of TANs from the target to the focal plane of TASCA, while suppressing transmission of beam and unwanted reaction products. By doing this, it is then possible to perform, e.g., chemical investigations, nuclear structure and nuclear reaction studies of the most neutron-rich nuclides.

TASCA was commissioned using reactions with nanobarn or larger cross sections [3, 4]. Therefore, the extension of TASCA experiments to picobarn-level cross sections remained the final step in the commissioning phase. To investigate a reaction with picobarn level-cross sections, a new detection and electronics system was developed for

TASCA [5]. As one of the first crucial tests of the performance of this system, when coupled to TASCA, we chose to investigate the 2*n* exit channels of ^{48}Ca-induced reactions on $^{206\text{-}208}$Pb to produce $^{252\text{-}254}$No. These reactions have cross sections on the order of microbarns [6], leading to expected production rates of atoms per second. These reactions have also been extensively studied at several recoil-separators including the Berkeley Gas-filled Separator (BGS) [7-9], the Dubna Gas-Filled Recoil Separator (DGFRS) [6], the gas-filled recoil separator RITU [10], the Fragment Mass Analyzer (FMA) [11], the velocity-filter SHIP [12-14], and the energy-filter VASSILISSA [15]. This allows for a comparison of the cross sections measured at TASCA to those measured at other recoil separators, giving an indication of the efficiency of TASCA for these reactions. Decay properties of $^{252\text{-}254}$No include α-decay, spontaneous fission (SF), and electron capture branches, allowing for the characterization of the detection and data acquisition system using multiple different decay scenarios. In addition, α-decays of ^{253}No are in prompt coincidence with three intense γ-lines [16], ideal for testing TASCA's ability to be used in nuclear structure studies [17].

After establishing the new detection setup coupled to TASCA for the ^{48}Ca+$^{206\text{-}208}$Pb reactions, an extension of TASCA commissioning experiments towards reactions that have lower production rates was undertaken. For this purpose, the ^{244}Pu(^{48}Ca,3-4*n*)$^{289\text{-}288}$114 reaction, with a published cross section of $1.7^{+2.5}_{-1.1}$ pb and $5.3^{+3.6}_{-2.1}$ for the 3 and 4*n* exit channels [18], respectively, was investigated. The 3*n* exit channel of this reaction was first reported in 1999 when a collaboration working at the DGFRS published a decay chain assigned to the observation of ^{289}114, an α-particle emitter with a half-life $t_{½}$ of 21 s [19]. Among the ^{289}114 daughters were the isotopes ^{285}Cn and ^{281}Ds, which were observed to decay via α-particle emission with lifetimes τ of 15.4 min and 1.6 min, respectively. The chain terminated in SF of ^{277}Hs 16.5 min later. Shortly following this, reports of the production of ^{288}114 in the ^{244}Pu(^{48}Ca,4*n*) reaction were published [20]. When ^{288}114 was observed as the α-decay daughter of the new isotope ^{292}116, as produced in the ^{248}Cm(^{48}Ca,4*n*) reaction, these reports were seemingly substantiated [21]. However, more recent work from the DGFRS, which produced

additional and more detailed data, led to reassigning decay chains that were originally attributed to ^{288}114. They are now ascribed to ^{289}114 [18] while the very first claimed ^{289}114 decay chain [19], was not reproduced. Further studies at the DGFRS using the ^{242}Pu(^{48}Ca,3-4*n*)$^{287-286}$114 and ^{244}Pu(^{48}Ca,3-4*n*)$^{289-288}$114 reactions led to new types of decay chains being assigned to ^{286}114, ^{287}114 [22] and ^{288}114 [18]. The current body of acquired DGFRS data interpreted by the DGFRS group is summarized in [23].

In 2009, the ^{48}Ca+^{242}Pu reaction was studied at the BGS [24]. One atom of ^{287}114, produced in the 3*n* evaporation channel, and one atom of ^{286}114, produced in the 4*n* evaporation channel, were observed. These results provided the first confirmation of the production of decay patterns assigned to element 114, as well as a confirmation of the decay properties assigned to ^{286,287}114. The original reported cross sections were $1.4^{+3.2}_{-1.2}$ pb each, but were later revised to $3.1^{+4.9}_{-2.6}$ pb [25], in agreement with cross sections reported by Oganessian et al. [22]. We undertook to investigate the ^{244}Pu(^{48}Ca,3-4*n*)$^{289-288}$114 reactions with the goal of i) demonstrating the ability of TASCA to perform experiments with picobarn level cross sections and ii) providing a first confirmation the production of element 114 with ^{244}Pu targets and ^{48}Ca beams. Here we report on results of test experiments with ^{48}Ca beams and $^{206-208}$Pb targets, present an extended discussion of the experimental setup and include additional results on the ^{48}Ca+^{244}Pu reaction, part of which was previously published in [26].

II. EXPERIMENTAL

A pulsed (5 ms on/15 ms off) beam of ^{48}Ca^{10+} was extracted from an ECR ion source and accelerated by the UNIversal Linear ACcelerator (UNILAC) at the GSI to laboratory-frame energies of 231.2, 254.6 and 259.4 MeV. The beam passed through an induction coil prior to the entrance of TASCA to measure the beam intensity in a non-destructive way. A schematic of the TASCA setup is shown in Fig 1. The vacuum of the beam line was separated from the 80-Pa helium gas in TASCA using a window-less three-stage differential pumping system. For portions of the 259.4-MeV run and the entire

254.6-MeV run, a 55 μg·cm^{-2}-thick carbon stripper foil was mounted directly upstream of the target to increase the charge state of the beam. During these irradiations, the beam energy was increased to compensate for the energy loss inside the stripper foil. The beam then passed through a (2.22±0.05)-μm thick Ti target backing before entering the targets. Three arc-shaped target segments were mounted on a target wheel, which rotated synchronously with the beam macrostructure. For the 231.2-MeV irradiation, targets with average thicknesses of 558-μg·cm^{-2} ^{206}PbS, 522-μg·cm^{-2} ^{207}PbS, and 531-μg·cm^{-2} ^{208}PbS were used. All PbS targets were covered with 10-μg·cm^{-2} ^{nat}C. At ^{48}Ca beam energies of 259.4 and 254.6 MeV from the UNILAC, $^{244}PuO_2$ targets (isotopic composition: 97.9% ^{244}Pu; 1.3% ^{242}Pu; 0.7% ^{240}Pu; <0.1% other) were irradiated. A summary of the experiments, beam energies and doses can be found in Table I. The $^{244}PuO_2$ targets were prepared on (2.22±0.05)-μm thick Ti foils by electrochemical deposition from isobutanolic solution [27], a procedure that yielded the oxide form after annealing. Over the course of the experiment, four ^{244}Pu target segments with a beam dose weighted average target thickness of 438-μg·cm^{-2} ^{244}Pu (as 495-μg·cm^{-2} $^{244}PuO_2$) were irradiated with typical beam intensities of $2\cdot10^{12}$ particles·s^{-1}.

Energy losses in carbon, titanium and lead sulfide ($^{206-208}$PbS) were calculated with SRIM2008 [28]. Beam energies inside the ^{207,208}PbS targets were 212.3-217.0 MeV. Inside the ^{206}PbS target, the beam energy range was 212.0-217.0 MeV. Compound nucleus excitation energies were calculated using beam energies with experimental mass defects for ^{48}Ca, $^{206-208}$Pb, and $^{252-254}$No [29]. Excitation energy ranges inside the targets were 21.2±2.0, 20.7±1.9, and 20.5±1.9 MeV for ^{206}PbS, ^{207}PbS, and ^{208}PbS, respectively, where the error bars represent the range of excitation energies within the targets. Energy losses inside the $^{244}PuO_2$ were extrapolated from values calculated with SRIM2008 of ^{48}Ca in hypothetical $^{244}RnO_2$, $^{244}RaO_2$, $^{244}ThO_2$, and $^{244}UO_2$ to $^{244}PuO_2$. Beam energies inside the $^{244}PuO_2$ target material were initially 241.3-246.2 MeV and then later decreased to 236.4-241.0 MeV. Compound nucleus excitation energies were calculated using beam energies with experimental mass defects for ^{48}Ca and ^{244}Pu [29] and Thomas-Fermi mass defects for the compound nucleus [30]. Resulting ranges of compound

nucleus excitation energies within the $^{244}PuO_2$ targets were $41.7^{+2.2}_{-1.9}$ and $37.5^{+2.0}_{-1.4}$ MeV, where 41.7 and 37.5 represent the excitation energy at the beam-dose weighted center of the target and the error bars represent the average spread in energies in the target.

Compound nucleus evaporation residues (EVRs) are formed with the momentum of the beam and recoil out of the target and into TASCA. TASCA comprises a DQQ magnet configuration, where D denotes a dipole magnet and Q a quadrupole magnet [1]. EVRs were separated from the beam and other unwanted reaction products in TASCA based upon their differing magnetic rigidities $B{\cdot}\rho$ in the 80-Pa helium gas. For the 231.2-MeV irradiation of the $^{206\text{-}208}$Pb targets, TASCA was set to center EVRs of 2.10 T·m in the focal plane. When ^{206}Pb targets were irradiated, $B{\cdot}\rho$ settings of 2.22 and 1.98 T·m were also used to move the implantation of SF-decaying ^{252}No EVRs to the edges of the detector. For the first part of the element 114 run, at 259.4-MeV, magnetic rigidities of the element 114 EVRs were estimated as described in [7] and accordingly, TASCA was set to center EVRs with a $B{\cdot}\rho$ of 2.23 T·m in the focal plane. After observation of the position of the first 10 events, the centered $B{\cdot}\rho$ was increased to 2.28 T·m.

TASCA is designed to be operated with the dipoles polarized either as Q_VQ_H or Q_HQ_V, where the indices indicate vertical (V) or horizontal (H) focusing [1]. This allows for choosing between two different focal plane image sizes, each with different EVR transmission efficiencies. When polarized as Q_HQ_V, the efficiency of TASCA ε_{TASCA} for the transmission of EVRs to the focal plane is increased, and the focal plane image is more dispersed. For the majority of the run, TASCA was operated in this High Transmission Mode (HTM) to maximize the rate of 114 events. However, for part of the run, TASCA was operated in the Q_VQ_H configuration, referred to as the Small Image Mode (SIM). In this mode, the focal plane image is significantly smaller than in the HTM, which comes at the cost of reduced EVR transmission efficiency. The use of SIM was done to determine the feasibility of future experiments on the chemistry of element 114.

A. TASCA efficiency

ε_{TASCA} is limited by i) the initial position, energy, and angular distribution of recoils exiting the target, and ii) the transmission of these recoils through TASCA. The latter is limited by the influence of the magnetic fields on the recoils, as well as their energy loss, multiple scattering, and charge exchange in the He fill gas. All of these effects, together with the effects of the estimated angular and energy distributions of the ^{48}Ca beam entering TASCA were calculated with a Monte Carlo simulation first developed for the BGS and later adapted for TASCA [7, 31, 32]. In this simulation, the initial ^{48}Ca beam energies and directions were chosen from assumed Gaussian energy and Gaussian angular distributions. The Gaussian energy distributions for the ^{244}Pu irradiation had a full-width at half-maximum (FWHM) of 0.2% (a typical beam energy uncertainty from the UNILAC) and centroids c of 243.8 and 238.7 MeV for the 259.4-MeV and 254.6-MeV irradiations, respectively, chosen to put c at the center of the targets with an estimated sigma s of 4 MeV for both irradiations. The Gaussian angular distributions had a FWHM=0.9° – typical for the beamline leading to TASCA. The beam energy was corrected for energy loss in the target backings. Points were randomly chosen from the assumed Gaussian excitation function with centroids positioned at the center-of-target beam energies. Variation in both backing and target thickness were taken into account using assumed thickness distributions approximated by the shape of a house with a peaked roof. If those points were within the energy range subtended by the target (thickness=(503±50)-μg/cm^2 $^{244}PuO_2$, dE/dx=8.3 MeV/(mg·cm^{-2})], the depth of interaction in the target was calculated, and a simulation of the trajectory of an EVR was initiated. The initial energy and angle of the EVR in the laboratory frame were corrected for the effect of isotropic (center-of-mass frame) evaporation of 3 or 4 neutrons, with the assumption that each neutron is emitted with 2-MeV of kinetic energy. Energy loss and angular scattering in the remaining target material was calculated for each EVR using SRIM2008 [28]. After exiting the target, trajectories through TASCA were simulated, including effects of magnetic fields, charge exchange in the gas [7], scattering in the gas [33], and energy loss in the gas [28]. By comparing the number of EVRs reaching the focal-plane detector in the simulation with the initial number of ^{48}Ca beam particles, effects of the fraction of the excitation function contained in the target and of ε_{TASCA} as a function of target depth were accounted for. Fig. 2 contains horizontal and vertical cross

sectional views of predicted element 114 EVR trajectories inside TASCA during HTM operation. ε_{TASCA} is estimated to be (60±6)%, (59±6), and (35±4) for the 259.4-MeV HTM, 254.6-MeV HTM and 259.4-MeV SIM runs, respectively. Beam doses of $2.44 \cdot 10^{18}$ (259.4-MeV HTM run), $1.15 \cdot 10^{18}$ (254.6-MeV HTM run), and $1.00 \cdot 10^{18}$ (259.4-MeV SIM run) particles were acquired. The uncertainty in the beam dose is 9% and is described in more detail in Section III.F. Similar calculations were performed for irradiations of the $^{206\text{-}208}$Pb targets and ε_{TASCA} was estimated to be (56±6)% for the $^{206\text{-}208}$Pb(^{48}Ca,2*n*) reactions. ε_{TASCA} values for all of the experiments in this work can be found in Table I.

B. Detection setup

After separation in TASCA, the element 114 EVRs passed through a multiwire proportional counter (MWPC) and were implanted into a focal plane detector (FPD). The MWPC was located ~27 cm upstream of the FPD and consisted of two 0.25-μm thick Mylar windows isolating an isobutane fill gas, held at a pressure of 400 Pa. No time-to-amplitude converter was used to give timing information between the MWPC and FPD. The output signal from the MWPC was divided after a preamplifier in two: i) from one a logical signal was created using a timing filter amplifier and a constant fraction discriminator; ii) the another one was amplified by a spectrometric amplifier and digitalized in an ADC. Both the logical signal and the digitalized amplitude were read out as part of the event triggered by any signal from the FPD and were used to allow for differentiation between implantation events and decays within the FPD.

The FPD was composed of an implantation detector (ID) and an upstream detector. The ID consisted of two 300-μm thick, 72 x 48 mm^2 Double Sided Silicon Strip Detectors (DSSSD). The front side of each DSSSD contained 72 vertical strips with a 1 mm pitch and 900-μm wide strips giving the position of the events along the X-axis (hereafter referred to as the StopX strips). The back side of the DSSSD consisted of 48 horizontal strips with a 1 mm pitch and 500-μm wide strips, giving the position of the events along the Y-axis (hereafter referred to as the StopY strips). Overall, the ID comprised 144 vertical strips and 48 horizontal strips. The geometric efficiency of the DSSSD for

registering events being implanted into the detector with both X- and Y- coordinates was 90% [5]. To discriminate decay-like events (events anticoincident with a signal from the MWPC) from signals due to light and low-ionizing particles (e.g., H^+, He^+, He^{2+} from interactions of the beam with the He fill-gas), which pass through the MWPC undetected and deposit a similar amount of energy in the FPD, two 500-μm thick, 72 x 48 mm^2 Single Sided Silicon Strip Detectors (SSSSDs) were mounted directly behind the ID. A signal in any of these 'punchthrough detectors' indicates light and low-ionizing particles. Fig. 3 contains spectra of all events with E<10 MeV during the 259.4-MeV HTM run as well as events with E<10 MeV during the 259.4-MeV HTM run that were anticoincident with the punchthrough detectors. As can be seen in the figure, the punchthrough detectors provided background suppression mainly in the region of 1-3 MeV, which is the typical energy deposited in 300-μm thick silicon by light and low ionizing particles.

Eight additional 500-μm thick, 72 x 48 mm^2 SSSSDs were mounted perpendicular to, and upstream of, the ID to form a five-sided box configuration as shown in Fig. 1. Each SSSSD had eight 5.75-mm wide strips with a 6 mm pitch. These 'upstream' detectors allowed for detecting α-particles and SF fragments that escaped from the ID, thus significantly enhancing the α-particle detection efficiency and allowing for registering the full energy of both fragments of SF events. Data acquisition was triggered by any event registering more than ~300 keV in a DSSSD or more than ~500 keV in a SSSSD. The efficiency for detecting α-particles was 72% of 4π. 50% of all α-particles deposit their full energy in the ID. An additional 22% of α-particles lose a fraction of their energy in the ID and hit an upstream detector. Their full energy can thus be reconstructed by summing the signals in both the implantation and upstream detectors. Of the remaining 28% of all α-particles, most escape out of the front of the detector box at an angle that leads to deposition of 300-500 keV in the FPD due to a shallow implantation depth and the 0.6-μm deadlayer on the detectors. The FPD was calibrated in the absence of beam with an external four-line α-particle source (^{148}Gd, ^{239}Pu, ^{241}Am, ^{244}Cm). The calibration was monitored on-line during the 254.6- and 259.4-MeV runs using α-decays from the implanted transfer reaction products (TRPs) ^{214g}Fr (α-particle energy E_α=8427 keV) and ^{212m}Po (E_α=11650 keV).

Due to the spacing between StopY strips of the ID, ~13-20% of events (depending on energy) were split between two neighboring StopY strips. Energy splitting between neighboring StopX strips was only observed in 0.008% of events. To be considered correlated, all events within a decay chain were required to be in the same StopX strip and either in the same StopY strip or split between the same two neighboring StopY strips, hereafter referred to as a 'pixel'.

One germanium cluster detector [34] with seven independent germanium crystals was mounted behind the 3 mm-thick Al backplate of the TASCA detection chamber, such that the germanium crystals were positioned about 2 cm behind the ID. A standard ^{152}Eu γ-ray source was used for γ-ray energy calibrations. The α-γ coincidence source ^{241}Am, as well as α-γ coincidences following the ^{207}Pb(^{48}Ca,2n)^{253}No reaction were used to produce prompt α-γ correlations between the FPD electronics and the 8-channel sampling ADC used to process the germanium-detector signals.

The status of the beam pulse (whether beam was or was not being delivered to TASCA) was recorded by a flag in each event in the data, which provided no information on the time since the start (or stop) of the beam pulse. As such, there was an inherent uncertainty in the time each beam pulse began and ended proportional to 1/(data rate). The UNILAC delivers beam pulses at a rate of 50 Hz (sometimes an experiment gets <50 Hz due to beam sharing), meaning that a new beam pulse should begin 20 ms after the start of the preceding pulse. The actual time difference between the start of individual beam pulses varies by up to 0.1 %, in an unpredictable manner. Due to this and the number of beam pulses required to obtain statistics (~10 events are implanted in the FPD during each 5-ms beam pulse), the beginning of an individual beam pulse could not be estimated within <100 μs.

C. Correlation Search conditions

Decay properties of $^{252\text{-}254}$No and their daughters $^{248\text{-}250}$Fm are well known [35]. ^{252}No (α-branching ratio B_α=0.731: E_α=8.42, α-particle intensity I_α=0.25; E_α=8.37 MeV I_α=0.75; B_{SF}=0.269, $t_{½}$=2.30 s [35]) and its daughter ^{248}Fm (B_α=0.93: E_α=7.87, I_α=0.8; E_α=7.83 MeV I_α=0.2; $t_{½}$=36 s [35]) are both short-lived isotopes with significant α-decay branches. ^{252}No also has a significant SF branching ratio. This allowed for the use of four semi-independent methods of calculating the amount of ^{252}No in the FPD:

i) Integral of ^{252}No-like α-particles [8.25<E_α(MeV)<8.55].

ii) EVR-α correlations consisting of an EVR [5.0<E_{EVR}(MeV)<12.0, coincident with the beam pulse and MWPC] followed within 6.9 s (three times the 2.3-s ^{252}No half-life)by an α-like particle (as described in i) within the same pixel.

iii) EVR-α-α correlations consisting of an EVR-α correlation (as described in ii) and followed within 108 s (three times the 36-s ^{248}Fm half-life) by an *a*-like particle [7.7<E_α(MeV)<7.95] within the same pixel.

iv) EVR-SF correlations consisting of an EVR [5.0<E_{EVR}(MeV)<12.0, coincident with the beam pulse and MWPC] followed within 6.9 s by a SF-like event [80<E_{SF}(MeV)<300, E_{ID}<200 MeV, anticoincident with the beam pulse and MWPC] in the same pixel.

All events were required to be anticoincident with the punchthrough detectors. All α-like events were required to be anticoincident with the MWPC and to occur outside of the beam pulse, where the background from low-ionizing particles was greatly reduced. α-like events were also required to have their full energy deposited in the ID due to the better energy resolution and lower background associated with those events.

^{253,254}No are longer-lived, predominately α-decaying isotopes (^{253}No: $t_{½}$=1.7 min, E_α=8.010 MeV, ^{254}No: $t_{½}$=55 s, E_α=8.093 MeV) with longer-lived α-decaying daughters (^{249}Fm: $t_{½}$=2.6 min, E_α=7.527 MeV, ^{250}Fm: $t_{½}$=30 min, E_α=7.430 MeV). Due to the rate of ^{253,254}No-like α-particles [7.85<E_α(MeV)<8.25, anticoincident with beam pulse and MPWC, full energy deposited in ID] and the rate of EVR-like events [5.0<E_{EVR}(MeV)<12.0, coincident with beam pulse and MWPC], ~1-3 random EVR-like events are expected to be correlated to each $^{253\text{-}254}$No-like α-decay within 3 average half-

lives of ^{253,254}No. As such safely correlating a ^{253,254}No-like α-particle to a nonrandom EVR was not possible. The amount of ^{253,254}No implanted in the FPD was determined based on the integral of ^{253,254}No-like α-decays with their full energy deposited in the ID that occurred outside of the beam pulse, where the background in the α-particle energy region was significantly lower.

Decay properties assigned to ^{288,289}114 as measured at the DGFRS have been previously published [23]. Guided by these results, we searched for time- and position-correlated decay chains consisting of an EVR, one or more α-like events and terminating with a SF. Element 114 EVRs were defined as events during the beam pulse with $3.0<E_{EVR}(\text{MeV})<15.0$, coincident with a signal from the MWPC and anticoincident with the punchthrough detectors. α- and SF-like events were anticoincident with both the MWPC and punchthrough detectors. α-like events could occur either inside or outside beam pulses. For portions of the experiment, the terminating SF was required to occur outside of the beam pulse.

^{288}114 was identified by detection of EVR-α-SF correlations that consisted of an EVR followed by an α-particle [$9.7<E_{\alpha}(\text{MeV})<10.2$] within 7 s and a terminating SF within 1 s. ^{289}114 was identified by EVR-α-α-SF correlations that consisted of an EVR followed by an α-particle [$9.7<E_{\alpha}(\text{MeV})<10.2$] within 7 s, a subsequent α-particle [$9.0<E_{\alpha}(\text{MeV})<9.5$] within 150 s and terminated by SF within 50 s of the last α-particle. We also searched for additional EVR- or α-like [$8.0<E_{\alpha}(\text{MeV})<12.0$] events between the EVR beginning the chain and the terminating SF. Direct SF of ^{288,289}114 was not searched for due to the high rate of SF-like events. A summary of all search conditions for $^{252\text{-}254}$No and $^{288\text{-}289}$114 are contained in Table II.

III. RESULTS AND DISCUSSION

A. Characteristics of the detectors

The $^{206\text{-}208}$Pb(^{48}Ca,2n)$^{252\text{-}254}$No reactions were primarily used to check the transmission of TASCA, the energy calibration of the FPD and to derive proper selection criteria on

signals from the electronics. In the presence of beam, the FPD was calibrated using reactions of ^{48}Ca with ^{206,208}Pb. The energy resolution was 25 keV FWHM for 8.1 MeV α-particles depositing their full energy in the ID. For α-particles that deposited a fraction of that energy inside the ID and the remainder in the upstream detector, the FWHM for an 8.1 MeV α-particle was 170 keV. This large FWHM is due to the wide variety of angles with which the α-particle can leave the ID and still implant in the upstream detector. As the upstream detectors are not position sensitive, the angle of escape was not accurately known, making deadlayer corrections on an event-by-event basis impossible. The calibration of the upstream detectors was checked using reconstructed α-particles from the ^{208}Pb(^{48}Ca,2n)^{254}No reaction.

During the $^{206-208}$Pb irradiations, low-energy tailing of α-lines of implanted nuclei formed in transfer reactions was noticed. Due to the comparatively long lifetimes of $^{252-254}$No and their daughters, corrections were not necessary to the α-particle energies during the 231.2-MeV irradiation. Throughout the 254.6- and 259.4-MeV irradiations of the ^{244}Pu targets, a wide variety of TRPs reached the TASCA FPD, besides the EVRs of interest. The half-lives of several of these products (^{220}Ra: $t_{½}$=18 ms, E_{α}=7686 keV; ^{215}At: $t_{½}$=0.1 ms, E_{α}=8024 keV; ^{219}Fr: $t_{½}$=20 ms, E_{α}=7312 keV; ^{214g}Fr: $t_{½}$=5.0 ms, E_{α}=8427 keV; ^{218}Rn: $t_{½}$=35 ms, E_{α}=7129 keV; ^{216}Rn: $t_{½}$=45 μs, E_{α}=8050 keV; ^{216}Po: $t_{½}$=0.145 s, E_{α}=6778 keV; ^{214}Po: $t_{½}$=164 μs, E_{α}=7686 keV) were sufficiently short that deviations in the energy of the α-particles were noticeable. These deviations were found to be a function of the energy of the event in the same strip that preceded the α-particle and the time difference between the α-particle and its preceding event, as can be seen in Fig. 4. Sufficient data were available to apply corrections to low energy events preceded by events with energies of i) ~6-9 MeV where α-α correlations of TRPs could be analyzed and ii) 40-60 MeV through recoil-α correlations as TRP recoils are formed with twice the momentum of the beam and implant into the detector with these energies. Corrected (right) and uncorrected (left) spectra are contained in Fig. 4 for α-particles preceded by events with energies of 40-60 MeV (top) and 6-9 MeV (bottom). Where sufficient data existed, a correction of all low energy (<15 MeV) events was made to

account for these energy deviations. No energy correction was necessary for any event contained in the $^{288\text{-}289}$114 chains.

The high-energy calibration used for measuring fission fragment energies was obtained from extrapolating the calibration from the α-energy region. This calibration was tentatively verified using SF events produced in the ^{206}Pb(^{48}Ca,2n)^{252}No reaction. However, insufficient data were obtained for a more accurate calibration. The high-energy calibration of the upstream detector was rather poor due to the lack of high-statistics calibration data.

During portions of the ^{244}Pu(^{48}Ca,3-4*n*) experiment (~67%), pinholes and/or rips in the targets allowed a fraction of the $^{48}Ca^{10+}$ beam to enter TASCA in the initial 10+ charge state without being stripped inside the target backing and target material. During the other 33% of the irradiation, where target integrity was not compromised, an estimated 100 ^{48}Ca beam particles per second left the target with a 10+ charge state. A fraction of this $^{48}Ca^{10+}$ (5-10%) was then directed to the FPD by TASCA. Since the MWPC was only ~99% effective at distinguishing a $^{48}Ca^{10+}$ passing through, a portion of the beam approximated SF events. To differentiate between SF events and events originating from the ^{48}Ca beam, the ^{206}Pb(^{48}Ca,2*n*) reaction was used to produce ^{252}No ($t_{½}$=2.3 s) which has a SF branching ratio of 26.9% [35]. Spectra of MWPC signals for all high-energy [80<*E*(MeV)<250] events correlated within 10 s to EVR-like events [3<E_{EVR}(MeV)<15] during the ^{206}Pb(^{48}Ca,2*n*)^{252}No experiment are shown in Fig. 5. In correlations involving high-energy events that were outside of the beam pulse, the recorded MWPC signal was peaked at ~150 channels and extended out to ~200 channels. The time difference between the high-energy events and their associated recoils were plotted (see Fig. 5 insert) and a half-life of ~2.2 s for these correlations was observed, indicating that they are due to the SF decay of ^{252}No. When the high-energy event occurred inside of the beam pulse, the MWPC signals peaked around 310 channels, with shoulders at ~250 and ~500 channels. A separate, significantly smaller peak occurred between 100-200 channels. Further analysis of the events in the peak below 200 channels showed that they decayed with a lifetime of ~2.1 s, characteristic of ^{252}No (see Fig. 5 insert), while events

in the peak at ~310 channels did not decay with a characteristic lifetime, indicating that they were components of background. As such, the threshold for a valid MWPC signal was set at 200 channels. SF and α events were required to have MWPC signals below 200 channels, while EVRs were required to have signals above 200 channels.

While requiring SF events to be anticoincident with the MWPC significantly reduced the number of beam particles approximating SF events, the distribution of MWPC signal from beam particles entering the FPD is broad enough that a fraction of beam particles (~1 %) have MWPC signals <200 channels. To further distinguish beam- and SF events, the energy distribution of the ID portion of high-energy events from correlations between EVRs and high-energy events in the ^{206}Pb(^{48}Ca,2*n*) reaction were analyzed, with the spectra being shown in Fig. 6. For high-energy events that occurred inside the beam pulse, and attributed in the previous paragraph to ^{48}Ca beam entering the FPD, a peak occurs at 190 MeV with a FWHM of 13 MeV and a significant low-energy tail. The high-energy events outside of the beam pulse (attributed to ^{252}No) had a broad peak centered around 140 MeV. This energy difference was used to further distinguish SF events by requiring the energy in the ID E_{ID} be <175 MeV if the SF event occurred inside of the beam pulse, reducing the detection efficiency of inside-the-beam pulse SF events by 13%.

For the ^{244}Pu(^{48}Ca,3-4*n*) reactions, the energy of the ^{48}Ca beam was 25-30 MeV higher than that used in the ^{206}Pb(^{48}Ca,2*n*) reaction at the center of the target. After taking into account pulse height defects, the peak from scattered beam was expected to occur around 220 MeV in the ^{244}Pu(^{48}Ca,3-4*n*) reactions. Various theories [36, 37] predict that the total kinetic energy (TKE) of the SF of ^{277}Hs, ^{281}Ds, and ^{284}Cn is ~30 MeV higher than the TKE of ^{252}No, indicating ID energies centered around 150 MeV. Due to this, SF events were defined as events with $80<E_{SF}(\text{MeV})<400$, $E_{ID}(\text{MeV})<200$ for all ^{244}Pu irradiations to maximize the efficiency for detecting SF-decays while minimizing the contribution of random SF-like events from ^{48}Ca beam. Even with this restricted definition of SF-like event, the rate of SF-like events during the beam pulse was 0.01-0.1 s^{-1} for 58% of the experiment, while an additional 5% and 4% of the experiment had

rates of 0.1-1 s^{-1} and >1 s^{-1}, respectively. As such, for portions of the run where background from the ^{48}Ca beam approximated SF-like events with a rate higher than 0.01 s^{-1}, SF events were required to occur outside of the beam pulse to reduce contributions from the low-energy tailing of the beam peak.

B. EVR image in TASCA

The ^{48}Ca beam entered the targets with a beam size of 6-mm diameter. Due to the momentum of the beam, EVRs are formed with a forward focus, although they experience scattering in the target. The large number of reaction products from the ^{48}Ca+^{206}Pb reactions allowed for a quantification of the effect of scattering in the 558-μg·cm^{-2} ^{206}PbS target and of the magnification of the EVR image in TASCA. Fig. 7 shows the position of ^{252}No decays at a magnetic rigidity setting of 2.10 T·m along with the distribution predicted by the Monte Carlo simulation of EVR trajectories (as described in Section II.A) in the HTM of TASCA. The experimental focal plane image had a FHWM of 58 mm in the horizontal direction and 22 mm in the vertical direction. This is slightly larger than that predicted by the simulations, likely due to scattering of the EVRs in the MWPC, which was not included in the simulation, but could indicate over- or underfocusing of the quadrupoles. For the SIM, the predicted and experimental position of ^{254}No decays is shown in Fig. 8. The simulation accurately predicts the distribution of ^{254}No decays, although insufficient data were available to determine position distributions for SIM.

During the experiment, the $B\cdot\rho$ of TASCA was changed to move the implantation ^{252}No events to the edges of the ID. This allowed for measuring the dispersion in TASCA (mm/(% change in $B\cdot\rho$)). It was determined to be 6.5 mm/(% $B\cdot\rho$). This is in slightly better than the 8±1 mm/(% $B\cdot\rho$) dispersion predicted by the TASCA simulations as described in Section II.A.

At a TASCA B·ρ setting of 2.10 T·m, the $^{252\text{-}254}$No EVRs were centered at strip 66.4±0.3. Based on the measured TASCA dispersion, this indicates that the $^{252\text{-}254}$No EVR B·ρ is (2.084±0.011) T·m. This is comparable to the ^{254}No B·ρ of 2.085 T·m that was measured

at the BGS with a helium pressure of 67 Pa, although slightly higher than the B·ρ of 2.04 T·m that was measured at GARIS [38].

C. The $^{206\text{-}208}$Pb(^{48}Ca,2*n*) $^{252\text{-}254}$No reactions

1. ^{252}No Decay properties

The half-life measured for ^{252}No based on ~8000 EVR-α and EVR-SF correlations was (2.47±0.02) s, in agreement with but more precise than literature values of $2.38^{+0.26}_{-0.22}$ s [15], (2.44±0.04) s [6], (2.30±0.22) s [39], (2.44±0.12) s [40] and (2.42±0.06) s [13] . The SF branching ratio was calculated to be (29.3±0.9)% which is comparable to literature values of (32±3)% [15], (32.2±0.5)% [6] and (26.9±1.9)% [39], although slightly larger than the value of (21.6±4.2)% from Andreyev *et al.* [41]. For ^{248}Fm, analysis of ~1000 EVR-α-α correlations yielded a half-life of (35.1±0.8) s, which is in good agreement with but more precise than the previously measured value of (36±3) s [35].

2. Cross sections

To examine TASCA's ability to accurately determine cross sections, excitation functions measured at the BGS [8], the DGFRS [6], SHIP [12-14] and VASSILISSA [15] were compared. To avoid discrepancies arising from comparing the TASCA data to measurements at single points rather than at the maximum of the excitation function, fits were performed on the data from each of the separators, employing a Gaussian on the low-energy side smoothly joined to an exponential tail on the high-energy side:

$$\begin{aligned} \sigma &= Ae^{-(E-c)^2/2w^2}, E \le \lambda w^2 + c \\ \sigma &= Ae^{\lambda^2 w^2/2} e^{-\lambda(E-c)}, E > \lambda w^2 + c \end{aligned} \quad (1)$$

where σ is the cross section as a function of the ^{48}Ca beam energy, *E*, *A* is the amplitude at the centroid, *c*, of a Gaussian with width, *w*, and λ is the exponential slope.

For the $^{206\text{-}208}$Pb(^{48}Ca,2*n*)$^{252\text{-}254}$No excitation functions, both a global and 'best' fits were done to determine the influence of varying λ and *w* on the maximum cross section. Before fitting, systematic errors were removed from the data as these errors are constant

for a given reaction and separator. For the global fit, λ and w values were fixed to 0.34 MeV^{-1} and 2.9 MeV, respectively, allowing only c and σ to vary until the solution converged. In the 'best' fit, all values were allowed to vary until the solution converged if sufficient data was available to fit the shape of the excitation function. The λ, w, c and maximum σ values for all data are contained in Table III. For TASCA, c was fixed to the c of SHIP, under the assumption differences in the energy at the peak of the excitation are due to systematic uncertainties energies from individual accelerators. In all cases, differences between the cross sections at maximum of the excitation function according to the global and 'best' fits differed by less than 6% (≤3% in 9 of 11 cases), indicating that the maximum cross section is stable over a range of ±10% for λ and w.

The ^{208}Pb(^{48}Ca,2n)^{254}No excitation functions, and their global fits, to the BGS [8], the DGFRS [6], SHIP [12, 14, 42] and VASSILISSA [15] data are shown in Fig. 9. The resulting cross sections at the maximum of the excitation functions were: (2250±350) nb, (2370±180) nb, (1760±60) nb and (1920±260) nb for the BGS, DGFRS, SHIP and VASSILISSA, respectively. The cross sections values for the two gas-filled separators (BGS and DGFRS) agree well. A similar agreement is observed in the cross section estimate for the two velocity filters (SHIP and VASSILISSA), however, the velocity filters measure a cross section that is ~22% lower than that measured at the gas-filled separators. This difference may indicate systematic over- or underestimates of transmission efficiencies through the different types of separators or the presence of a short-lived (>100 ns, <1 μs) isomer in ^{254}No. The decay of this isomer would change the ^{254}No charge state, reducing the transmission efficiency in the velocity filters, but not in the gas-filled separators.

For TASCA, the cross sections for the ^{208}Pb(^{48}Ca,2n) reaction was measured to be (1890±40) nb in the 231.2-MeV HTM irradiation and (1650±40) nb in the 231.2-MeV SIM irradiation, after correcting for the α branching ratio. The lower cross section in the 231.2-MeV SIM irradiation (which was performed after the 231.2-MeV HTM irradiation) indicates that some of the ^{208}PbS target material was lost due to sputtering or evaporation during the two experiments. A fit to the 231.2-MeV HTM irradiation, assuming the

SHIP λ, w and c values, indicates that the maximum cross section is (2000±140) nb. This value is lower than (although within 1 σ of) the cross sections measured at the other gas-filled separators. However, this is to be expected if an unknown amount of target material was sputtered or evaporated off the target during the irradiation.

A cross section of 760±10 nb was measured for the ^{207}Pb(^{48}Ca,2n) reaction using TASCA in the HTM. Excitation function measurements are also available for the DGFRS [6]. These data suggest that the maximum cross sections are (1130±170) nb and (870±10) nb at the DGFRS and TASCA, respectively. The fit to the DGFRS value is ~23% higher than the TASCA value, consistent with what was observed in the ^{208}Pb(^{48}Ca,2n) reaction and with the prior assumption of loss of target material during irradiation.

For the ^{206}Pb(^{48}Ca,2n) reaction, experimental data were available for the DGFRS [6], SHIP [13] and VASSILISSA [15]. A cross section of (310±10) nb was measured during the 231.2 MeV irradiation at TASCA. The resulting cross sections at the maximum of the excitation function were (500±40), (350±10), (430±10) and (320±30) for the DGFRS, TASCA, SHIP and VASSILISSA, respectively. The maximum cross section from the TASCA experiment is in agreement with the VASSILISSA data, but 19-30% lower than the cross sections from the DGFRS or SHIP. Again, this is an indication that target material is being lost during the irradiation.

Between the four separators, the maximum cross sections varied by 25-50% for the $^{206\text{-}208}$Pb(^{48}Ca,2n) reactions. The large deviation between measurements at individual separators indicates that there are difficulties in accurately measuring cross sections at or below the microbarn level.

D. α-γ coincidences

The ^{207}Pb targets were used to produce ^{253}No to cross check the γ-ray energy calibration and the timing correlation of the germanium cluster detector with the event trigger. During this test, ~1200 ^{253}No α-particles [7.9<E_α(MeV)<8.3, anticoincident with MWPC] were observed. Two γ-ray peaks at 222.2 and 279.2 keV were readily observed,

in agreement with the data from [16]. Nevertheless, a timely offline check of the ^{253}No data proved that the yield of these peaks in relation to the number of detected ^{253}No α-particles was too low given the expected detection efficiency of the cluster of some 15-20% at these γ-ray energies. This was corrected early on in the element 114 production run by changing a delay constant in the sampling ADC, and cross-checked with α-γ-coincidences arising from a standard ^{241}Am source.

E. The ^{244}Pu(^{48}Ca,3-4n)$^{288\text{-}289}$114 reactions

1. ^{288}114

Eleven EVR-α-SF chains observed in the ^{48}Ca+^{244}Pu reaction were assigned to the decay of ^{288}114 (events 2-8, 10-11, 14-15 in Table IV). Eight of these events were observed during the 259.4-MeV HTM irradiation and one additional event during the 254.6-MeV HTM irradiation. These were previously published in [26]. Two additional events were observed during the 259.4-MeV SIM irradiation. The half-life originating from these 11 decays is $0.52^{+0.22}_{-0.13}$ s for ^{288}114 and $0.11^{+0.05}_{-0.03}$ s for ^{284}Cn, in agreement with those published in [23]. The α-particle energy from the eight ^{288}114 decays in which the full α-particle energy was deposited in the ID is (9.95±0.03) MeV, in agreement with the (9.94±0.06) MeV observed in [23].

Two of the eleven observed ^{288}114 decay chains were recorded while TASCA was operated in the SIM. The observation of two chains is consistent with the reduced efficiency and beam dose. These results indicate that, even with the reduced transmission, using TASCA in the SIM to study the chemistry of element 114 is feasible.

2. ^{289}114

Four EVR-α-α-(α)-SF chains were observed during the HTM portion of the ^{48}Ca+^{244}Pu irradiation, two each at 259.4 and 254.6 MeV (events 1, 9, 12-13 in Table IV). Half-lives of $0.97^{+0.97}_{-0.32}$ s, 30^{+30}_{-10} s and 20^{+20}_{-7} s were observed for ^{289}114, ^{285}Cn, and ^{281}Ds, respectively. The half-life of ^{285}Cn is in agreement with that published in [23] and those for ^{289}114 and ^{281}Ds agree within 2 σ. All four ^{289}114 and ^{285}Cn decays resulted in the

full energy of the α-particle being deposited in the ID. Based on these decays, the α-particle energies of ^{289}114 and ^{285}Cn are (9.87±0.03) and (9.21±0.03) MeV, respectively. These are slightly higher than, but still in agreement with the α-particle energies observed in [23] of (9.82±0.05) and (9.15±0.05) MeV for ^{289}114 and ^{285}Cn, respectively.

Chain 1 from Table IV differs from all chains published in [23]. ^{281}Ds was previously observed to decay only by SF [20, 43]. We observed an EVR-α-α-SF chain consistent with the decay of ^{289}114. However, between the second α-particle and the SF decay, we observed an (8.727±0.025)-MeV α-particle with a lifetime of 5.688 s, followed 4.502 ms later by the terminating SF, resulting in an EVR-α-α-α-SF correlation. While the energy region around 8.685 MeV is near α-lines of background activities like ^{211m,212}Po a statistical analysis indicates that there is only a 0.1% probability that this α-particle is unrelated to the other members of the decay chain. We assigned this event to the α-decay of ^{281}Ds [26], followed by SF of the new isotope ^{277}Hs, a previously unknown nucleus with Z=108, which has been shown to be a deformed proton shell closure in lighter isotopes with N ~ 162 [44].

The observed lifetime of ^{277}Hs results in a half-life of 3^{+15}_{-2} ms, which is short compared to half-lives of lighter Hs isotopes, which are situated near the deformed neutron shell closure at N=162. Furthermore, these Hs isotopes have only been observed to undergo α-decay, with a conservative lower limit of $t_{1/2}$(SF) of the order of ten seconds [44, 45]. However, the short measured lifetime for ^{277}Hs is in good agreement with theoretical predictions for Hs isotopes based on the macroscopic-microscopic model [46], which list 46 ms (^{276}Hs) and 0.98 ms (^{278}Hs) for the neighboring even isotopes (odd isotopes were not calculated). The geometric mean of the predicted half-lives of the neighboring ^{276,278}Hs is 6.7 ms. The odd neutron in ^{277}Hs is expected to hinder SF decay by several orders of magnitude. A comparison of experimental [23] and theoretical [47] values for even-even copernicium isotopes, where more experimental data is available for such a comparison, suggests that theory overestimates partial SF half-lives near N ~ 170 by one

to two orders of magnitude, which thus seems to be the accuracy of these calculations. Respecting the huge variations of $t_{1/2}$(SF) with N – in the case of Hs isotopes with N between 152 and 184, the predicted [46, 47] $t_{1/2}$(SF) cover 17 orders of magnitude – and the accuracy of such predictions, the agreement between the geometric mean of the predicted half-lives of the neighboring ^{276,278}Hs (6.7 ms) and our measured lifetime (4.5 ms) is good.

Theory suggest that nuclei with N~170 are located in a region of minimum shell stabilization between the deformed neutron shell closure N=162 and the expected spherical shell closure at N=184 [48]. Only limited $t_{1/2}$(SF) data for this region is available, and so far none for elements where isotopes with N~162 are known. Our data point for ^{277}Hs continues the Hs isotopic chain, which covers the N=162 shell closure region well, towards more neutron-rich isotopes, see Fig. 10. It verifies the influence of this shell on $t_{1/2}$(SF). So far, SF has not been observed for any Hs with N>156, including the recently observed ^{273}Hs [25]. Its reappearance at N=169 demonstrates that stability toward SF due to the influence of this shell vanishes with increasing distance from N=162; at least until the N=170 region.

3. Coincident X- and γ-rays

Detection of characteristic X-rays following α-decay of any of the events in the 114 chains would allow for a direct determination of the atomic number of the decay product. During the ^{48}Ca+^{244}Pu irradiation, we searched for X- and γ-rays in coincidence with any decay in the ^{288,289}114 decay chains, with the exception of chain 1 in Table IV, where the detection of γ-ray coincidences was not yet working properly (see Sec. III.D). Prompt γ-rays were detected in coincidence with the SF events in 11 of the remaining 14 chains (chains 3, 6-15 in Table IV). Of those 11 SF events, eight had one γ-ray each, while the remaining three SF events were correlated to two γ-rays each, when add-back of neighboring germanium crystals was enforced. No X- or γ-rays were observed in prompt coincidence with any EVR implant or α-particle from the ^{288,289}114 decay chains.

4. Cross sections

The ^{244}Pu(^{48}Ca,*xn*) reaction was investigated at excitation energies of E^*=36.1-39.5 and E^*=39.8-43.9 MeV. Cross sections at E^*=36.1-39.5 were measured to be $8.0^{+7.4}_{-4.5}$ pb for the 3*n* exit channel and $2.8^{+4.2}_{-2.1}$ pb for the 4*n* exit channel [26]. At E^*=39.8-43.9 MeV cross sections were measured to be $3.5^{+3.3}_{-2.0}$ pb and $9.8^{+3.9}_{-3.1}$ pb for the 3*n* and 4*n* exit channels, respectively. Error bars include statistical uncertainties at the 68.3% confidence level and are calculated according to [49]. Fig. 11 shows cross sections for the 3*n* and 4*n* exit channels of the ^{244}Pu(^{48}Ca,*xn*) reaction for this work along with the excitation function predictions from [22]. Horizontal error bars represent the range of beam energies covered inside the target, while vertical error bars represent the uncertainties due to counting statistics and are presented at the 1σ level. Also included in Fig. 11 are the 3-4*n* cross sections observed at the DGFRS [18]. At E^*=39.8-43.9 MeV cross sections from this work are higher than those from E^*=38.9-43.0 in [18], although they agree within 1 σ. In addition, at E^*=36.1-39.5 MeV we observe a 3*n* cross section that is 4 times the 3*n* cross section reported in [18], although they also agree within 1 σ. This large difference may be in part due to the difference in irradiation energies used in this work and in [18] or the difficulties in accurately measuring small cross sections as discussed in Section III.C.2.

5. Magnetic Rigidity

The $B\cdot\rho$ of element 114 EVRs in 80-Pa He was measured to be (2.29±0.11) T·m in the 259.4-MeV HTM run, where the best statistics was obtained, based on the observed horizontal position of the element 114 events in the ID and the assumed TASCA $B\cdot\rho$ of 2.23 T·m. With the lower statistics in the 254.6-MeV HTM run, the $B\cdot\rho$ of element 114 EVRs in 0.8 mbar He was measured to be (2.29±0.15) T·m.

6. Background Contributions

Fig. 12 shows the total low [7≤E(MeV)≤12] and high [25≤E(MeV)≤250] energy spectra recorded in the ID during the HTM and SIM portions of the ^{48}Ca + ^{244}Pu run with a total accumulated beam dose of $4.59\cdot10^{18}$. The spectra of α- and SF-like events (as defined in Sections III.E.1 and III.E.2) in the ID, both during and outside of the beam pulse for the

SIM and HTM runs, are also included. Energies of α- and SF events within decay chains presented in Table IV are indicated. In the HTM high energy spectra (Fig. 10d), a peak due to scattered beam reaching the ID appears at ~225 MeV. The peak at ~50 MeV in both the HTM and SIM high energy spectra is due to the fraction of recoils from TRPs that are formed with twice the momentum of the beam, recoil out of the target and are guided to the FPD by TASCA. A small portion of EVRs from TRPs appear to occur outside of the beam pulse, a problem that was not remedied offline (as discussed in Sec. III.B). An additional peak occurs around 150 MeV in the SF-like events anticoincident with the beam pulse. These events are correlated to high energy recoils [$40<E_{recoil}$(MeV)<60] on the millisecond (<20 ms) timescale and were assigned to the decay of americium fission isomers produced in transfer reactions.

Low energy spectra for both HTM and SIM are dominated primarily by the α-decay of short-lived products from transfer reactions having $Z_{product}<Z_{target}$. Cross sections for the production of below-target TRPs have been published for the ^{48}Ca+^{248}Cm [50] and ^{48}Ca+^{238}U reactions [51, 52]. To determine suppression factors (the predicted number of TRPs expected to be produced/observed amount of TRPs in FPD) for both modes of TASCA, the expected direct production yields of ^{218}Rn, ^{219}Fr, ^{220}Ra and ^{212m}Po were estimated based on published data from [50-52]. The amount of ^{218}Rn, ^{219}Fr, ^{220}Ra in the ID was estimated based on EVR-α-α correlations. For ^{212m}Po, the amount implanting into the ID was estimated based on the number of counts in the 11.65 MeV α-particle peak above background. In all cases, α particles were required to deposit their full energy in the ID. The total number of ^{218}Rn, ^{219}Fr, ^{220}Ra and ^{212m}Po in the ID were corrected for efficiency of α-particle detection, α-branching ratio, intensity of the α-line, dead time of the detector between events and the number of half-lives that correlations were searched out for. In HTM, unwanted below-target TRPs are suppressed by a factor of ~700. In SIM, the suppression factor is increased to ~2000.

7. Random Rates

The number of expected random EVR-α-SF and EVR-α-α-SF correlations was calculated by taking the observed number of SF events and multiplying by the probability

of observing an EVR-α or EVR-α-α correlation in the same pixel preceding the SF within the predefined time window. The rate of EVR-, α- and SF-like events during and outside of the beam pulse during normal operations is shown in Table V. During the portions of the run with a large number of pinholes in one of the three target segments, the rate of α-like events increased by a factor of 10. The rate of SF-like events inside the beam pulse increased to 0.01-0.1 s^{-1} for 58% of the experiment, while an additional 5% and 4% of the experiment had rates of 0.1-1 s^{-1} and >1 s^{-1}, respectively. However, outside of the beam pulse, the rate of SF-like events did not increase. As such, for portions of the run when the rate of SF-like events in the beam pulse was >0.01 s^{-1}, SF-like events were required to occur outside of the beam pulse.

During the experiment, there were 426 SF-like events occurring outside of the beam pulse. With the caveat that SF events occurred out of the beam pulse, it was possible to widen the correlation search gates for ^{288,289}114. For ^{288}114, correlation gates were widened to EVR [3.0<E_{EVR}(MeV)<15.0] followed by an α-particle [8.0<E_α(MeV)<12.0] within 30 s and terminated by a SF-like event outside of the beam pulse and within 50 s of the α-particle. With these wide gates, we expected to observe 3.0 random correlations of unrelated events. A total of 15 chains were observed. 10 had decay properties similar to ^{288}114 and where thus assigned (see chains 2-3, 5-8, 10-11, 14-15 in Table IV). The remaining 5 chains were assigned to random correlations of unrelated events as a result of one or more of the following conditions: (i) alpha energy was more than 500 keV lower than energies from the DGFRS experiments, (ii) lifetime of parent alpha was more than 3 times the longest ^{288}114 lifetime from DGFRS experiments, or (iii) lifetime of fission event were more than 3 times the longest ^{284}Cn lifetime from DGFRS experiments.

For ^{289}114 we searched for EVR-α-α-SF correlations that consisted of an EVR [3.0<E_{EVR}(MeV)<15.0] followed by an α-particle [8.0<E_α(MeV)<12.0] within 30 s, a second α-particle [8.0<E_α(MeV)<12.0] within 150 s and terminated by a SF-like event outside of the beam pulse and within 50 s of the last α-particle. A total of 5 EVR-α-α-SF correlations were observed where 1.3 were expected due to random correlations of unrelated events. Four of the EVR-α-α-SF correlations had decay properties similar to

those published for ^{289}114 and were thus assigned (chains 1, 9, 12 and 13 in Table IV). The remaining correlation [EVR (E_{EVR}=8.88 MeV) – α-particle (E_α=11.89 MeV, τ_α=13.227 s) - α-particle (E_α=8.81 MeV, τ_α=109.602 s) – SF (165 MeV, τ_{SF}=6.05s)] was assigned to random, uncorrelated decays of TRPs due to their *a*-particle energies.

Based on the decay properties of chains ending with out-of-beam SF events, we narrowed the gates to search for chains ending with in-beam SF events. During the portions of the run considered 'low' background enough to extend this search, there were 15499 SF-like events. ^{288}114 was identified by detection of EVR-α-SF correlations that consisted of an EVR followed by an α-particle [9.7<E_α(MeV)<10.2] within 7 s and a SF within 1 s. ^{289}114 was identified by EVR-α-α-SF correlations that consisted of an EVR followed by an α-particle [9.7<E_α(MeV)<10.2] within 7 s, a second α-particle [9.0<E_α(MeV)<9.5] within 150 s and terminated by a SF-like event within 50 s of the last α-particle. Based on the number of correlations with out-of-beam SF events and the portion of the experiment during which in-beam SF could be correlated to, an additional 1.2 events were expected. One additional EVR-α-SF correlation was observed with an in-beam SF and narrow α-energy gates (chain 4 in Table IV).

The number of expected random decay chains using the narrowed α-energy gates and with the terminating SF outside of the beam pulse was $4\cdot10^{-4}$ and $2\cdot10^{-4}$ for ^{288}114 and ^{289}114, respectively. When including in-beam SF events, the number of expected random correlations with the narrowed α-particle energy gates increased to 0.02 and 0.05 for ^{288}114 and ^{289}114, respectively. Thus, it is unlikely that any of the 15 assigned chains is the result of random correlations of unrelated events.

For each chain, all events between the EVR and the terminating SF were checked for additional EVR- or α-like [8.0<E_α(MeV)<12.0] events. Chain 1 in Table IV contained an additional EVR between α-particles 1 and 2, in the same pixel as the decay chain. In addition to the extra EVR in chain 1, chain 13 also contains a 14.04 MeV EVR 124.336 s after the implantation of the EVR starting the chain. The rate of EVR-like events during

the run was 52 s^{-1} (206 s^{-1} inside of beam pulse) over the entire detector. With this rate, the probability of observing two additional EVRs within the 15 decay chains and in their respective pixels is 17%. Chain 1 also contains an 8.727 MeV α-particle that was assigned to the α-decay of ^{281}Ds. The rate of α-like events [8.0<E_α(MeV)<12.0] during the experiment was 2.29 s^{-1} over the entire detector. The probability that any one of the decay chains had contained a random α-like event is <0.1%. No other additional α-like events were observed in any of the other 14 decay chains.

The original element 114 discovery claim was based on the observation of a 34-min long EVR-α-α-α-SF chain [19]. We extended our correlation parameters to search for chains of similar type with α-particle energy windows of 500 keV and lifetime windows three times longer than the lifetimes observed in [19]. This led to search parameters of EVR-α-α-α-SF correlations consisting of an EVR [3.0<E_{EVR}(MeV)<15.0] followed by three subsequent α-particles with

1. 9.5<$E_{\alpha 1}$(MeV)<10.0, $\Delta t_{EVR\text{-}\alpha 1}$<90 s
2. 8.4<$E_{\alpha 2}$(MeV)<8.9, $\Delta t_{\alpha 1\text{-}\alpha 2}$<45 min
3. 8.6<$E_{\alpha 3}$(MeV)<9.1 , $\Delta t_{\alpha 2\text{-}\alpha 3}$<4.8 min.

The chain would then have to be terminated by a SF-like event outside of the beam pulse and within 50 min of the last α-particle ($\alpha 3$). Unfortunately, with these search conditions, the number of expected random correlations was too high to allow for identification of chains similar to those suggested in [19], which implies that our experiment was not sensitive to such decay-chains.

F. Systematic uncertainties

The systematic uncertainties result from four main contributions: (i) The uncertainty in the efficiency to guide EVRs to the FPD. For the ^{48}Ca + $^{206\text{-}208}$Pb reactions, this uncertainty has been estimated to be σ_{eff}/eff=10%, by a comparison of the size and shape of the modeled and experimental focal plane position distribution. Because the kinematics of the ^{48}Ca+^{244}Pu reaction are similar, σ_{eff}/eff=10% was used. (ii) The uncertainty in the target thicknesses. Target thickness measurements were performed for

each segment before and after irradiation. There were all integral and do not reflect inhomogeneous microscopic structures of the targets. Loss of target material during the run was estimated to occur during the first several hours of the run, after which the target thickness remained stable. Errors in the target thickness were estimated to contribute 10% to the systematic uncertainty based on pre- and post-experiment measurements of the target thickness for each individual target. (iii) The uncertainties of the beam doses during the experiment. These were estimated based on readings from an induction coil upstream of the target. The beam dose obtained from the induction coil was then normalized to readings that were periodically taken in a Faraday cup directly upstream of the target. Comparisons of beam intensity as measured in the induction coil and that given by the faraday cup showed an approximately 6% error. (iv) The Faraday cup is estimated to measure beam intensities to within 5%. (v) Both the Faraday cup and induction coil are upstream of the target. It is estimated at 95±5% of the beam that passed through the Faraday cup and induction coil also passed through the target. (vi) EVRs energy gates were chosen based on the observed distribution of $^{254\text{-}252}$No EVRs and the predicted difference between the initial $^{254\text{-}252}$No and 114 EVR energies as well as the predicted energy losses in the remaining target, MWPC windows and detector dead layer. $^{254\text{-}252}$No and 114 EVRs are formed at the center of the target with similar energies. Energies losses of the $^{254\text{-}252}$No and 114 EVRs were estimated from extrapolation from SRIM2008 of the hypothetical atoms of ^{254}As (Z=33) through ^{254}U (Z=92) to ^{254}No (Z=102) and ^{288}As through ^{288}U to ^{288}114 when passing through the remaining target, mylar windows of the MWPC and dead layer of the FPD. Estimated average $^{254\text{-}252}$No implantation energies were ~17% higher than those for 114 EVRs. The energy spread of 114 EVRs after passing through the remaining target, MWPC windows and FPD dead layer was also expected to be ~22% wider than the spread of ^{254}No EVRs. The $^{254\text{-}252}$No EVRs had an average recorded implantation energy (not corrected for pulse-height defect) of 8.8 MeV with a FWHM of 3.1 MeV. Based on this, the expected 114 EVR implantation energy was 7.1MeV, with a FWHM of 3.8 MeV. The lower limit for the 114 EVR energy gate was set to 3 MeV due to a large probability of observing random correlations to low energy noise below 3 MeV. Based on the extrapolations from SRIM2008, 99±5% of the EVR distribution was expected to have energies of

$3 \leq E_{EVR}(MeV) \leq 15$. Standard error propagation of these six main contributions results in an overall systematic uncertainty of 18% for cross sections measured with TASCA, which is slightly higher than published previously in [26] due to the inclusion of error from (v) and (vi).

IV. CONCLUSION

The performance of the recently-installed gas-filled recoil separator TASCA at the GSI and its new detection system was verified using beams of ^{48}Ca to irradiate targets of $^{206\text{-}208}$Pb leading to the production of $^{252\text{-}254}$No isotopes. These studies allowed for detailed analysis of the performance of the separator and electronics. Decay properties and production rates of the $^{252\text{-}254}$No isotopes were in agreement with literature data. In the HTM, the dispersion was determined to be 6.5 mm/(% Bρ).

The ^{244}Pu(^{48}Ca,3-4*n*) reaction was also studied at GSI using the TASCA. Fifteen decay chains were observed and assigned to ^{288,289}114. The measured half-lives were $0.97^{+0.97}_{-0.32}$ s, 30^{+30}_{-10} s, 3^{+15}_{-1} ms and 20^{+20}_{-7} s for ^{289}114, ^{285}Cn, ^{281}Ds and ^{277}Hs, respectively. For ^{288}114 and its daughters, ^{284}Cn and ^{280}Ds, half-lives of $0.52^{+0.22}_{-0.13}$ s for ^{288}114 and $0.11^{+0.05}_{-0.03}$ s, respectively, were observed. A maximum cross section of $9.8^{+3.9}_{-3.1}$pb was observed for the 4*n* evaporation channel at E^*=39.8-43.9 MeV. While, for the 3*n* cross section, a maximum of $8.0^{+7.4}_{-4.5}$ pb was observed at E^*=36.1-39.5 MeV. These cross sections and half-lives, as well as decay modes and α-particle energies, agree with those reported from the DGFRS collaboration [23]. The high cross sections and observation of two of the ^{288}114 decay chains in the SIM demonstrate that TASCA is ideal for use as a physical preseparator [53] in future studies of the chemistry of element 114. In addition, we observed a previously unobserved α-decay branch in ^{281}Ds, leading to the discovery of the isotope ^{277}Hs. The separation from TRPs in TASCA was ~700 in HTM and ~2000 in SIM.

ACKNOWLEDGEMENTS

We thank the ECR ion source and UNILAC staff for providing excellent and stable ^{48}Ca beams. H. Brand and the GSI Experimental Electronics department, H. Grösslhuber, G. Matheis, and R. Bühnemann from the machine shop at the institute of radiochemistry, TU Munich, as well as V. Gorshkov provided technical support. L. Stavsetra provided preliminary BGS results for the ^{48}Ca+^{242}Pu reaction prior to publication, which we gratefully acknowledge. This work was financially supported by the German BMBF (06MT247I, 06MT248, 06MZ223I); the Research Center "Elementary Forces and Methematical Foundations" (EMG); the GSI-F&E (MT/TÜR, MZJVKR); the Swedish Science Council; the U.S. D.O.E. under contract No. DE-AC02-05CH11231 and the NNSA under Contract No. DE-FC52-08NA28752; the Norwegian Research Council (project no. 177538); the Govt. of India-XIth five year plan project "TADDS".

References

[1] A. Semchenkov *et al.*, Nucl. Instrum. Methods B **266**, 4153 (2008).
[2] K. Morita *et al.*, J. Phys. Soc. Japan **73**, 2593 (2004).
[3] J. Khuyagbaatar, (to be published).
[4] A. Gorshkov, (to be published).
[5] A. Gorshkov, Doktors der Naturwissenschaften (Dr. rer. nat.) Thesis, Technische Universität München, 2010; http://www-wnt.gsi.de/kernchemie/images/pdf_dipl_diss/Diiss_Gorshkov_2010.pdf.
[6] Yu. Ts. Oganessian *et al.*, Phys. Rev. C **64**, 054606 (2001).
[7] K. E. Gregorich *et al.*, Phys. Rev. C **72**, 014605 (2005).
[8] J. B. Patin, Lawrence Berkeley National Laboratory Report No. LBNL-49593, 2002.
[9] J. M. Nitschke, R. E. Leber, M. J. Nurmia, and A. Ghiorso, Nucl. Phys. A **313**, 236 (1979).
[10] R.-D. Herzberg *et al.*, Nature **442**, 896 (2006).
[11] S. K. Tandel *et al.*, Phys. Rev. Lett. **97**, 082502 (2006).
[12] H. W. Gäggeler *et al.*, Nucl. Phys. A **502**, 561 (1989).
[13] B. Sulignano *et al.*, Eur. Phys. J. A **33**, 327 (2007).
[14] F. Heßberger *et al.*, Eur. Phys. J. A **43**, 55 (2010).
[15] A. V. Belozerov *et al.*, Eur. Phys. J. A **16**, 447 (2003).
[16] F. P. Heßberger, S. Hofmann, D. Ackermann, P. Cagarda, R.-D. Herzberg, I. Kojouharov, P. Kuusiniemi, M. Leino, and R. Mann, Eur. Phys. J. A **22**, 417 (2004).
[17] L.-L. Andersson *et al.*, Nucl. Instrum. Methods A **622**, 164 (2010).
[18] Yu. Ts. Oganessian *et al.*, Phys. Rev. C **69**, 054607 (2004).
[19] Yu. Ts. Oganessian *et al.*, Phys. Rev. Lett. **83**, 3154 (1999).
[20] Yu. Ts. Oganessian *et al.*, Phys. Rev. C **62**, 041604 (2000).
[21] Yu. Ts. Oganessian *et al.*, Phys. Rev. C **63**, 011301 (2000).

[22] Yu. Ts. Oganessian *et al.*, Phys. Rev. C **70**, 064609 (2004).
[23] Yu. Ts. Oganessian, J. Phys. G **34**, R165 (2007).
[24] L. Stavsetra, K. E. Gregorich, J. Dvorak, P. A. Ellison, I. Dragojevic, M. A. Garcia, and H. Nitsche, Phys. Rev. Lett. **103**, 132502 (2009).
[25] P. A. Ellison *et al.*, Phys. Rev. Lett. **105**, 182701 (2010).
[26] Ch. E. Düllmann *et al.*, Phys. Rev. Lett. **104**, 252701 (2010).
[27] K. Eberhardt *et al.*, Nucl. Instrum. Methods A **590**, 134 (2008).
[28] J. F. Ziegler, Nucl. Instrum. Methods B **219-220**, 1027 (2004).
[29] G. Audi, O. Bersillon, J. Blachot, and A. H. Wapstra, Nucl. Phys. **A729**, 3 (2003).
[30] W. D. Myers and W. J. Świątecki, Lawrence Berkeley National Laboratory Report No. LBNL-36803, 1994); http://ie.lbl.gov/txt/ms.txt.
[31] K. E. Gregorich *et al.*, Eur. Phys. J. A **18**, 633 (2003).
[32] K. E. Gregorich *et al.*, GSI Helmholtzzentrum für Schwerionenforschung Report No. NUSTAR-SHE-10, 2006.
[33] J. P. Biersack and L. G. Haggmark, Nucl. Instrum. Methods **174**, 257 (1980).
[34] J. Eberth, H. G. Thomas, P. v. Brentano, R. M. Lieder, H. M. Jäger, H. Kämmerfing, M. Berst, D. Gutknecht, and R. Henck, Nucl. Instrum. Methods A **369**, 135 (1996).
[35] *Table of Isotopes*, edited by R. B. Firestone and V. S. Shirley (John Wiley and Sons, New York, 1996).
[36] V. E. Viola and G. T. Seaborg, J. Inorg. Nucl. Chem. **28**, 741 (1966).
[37] V. E. Viola, K. Kwiatkowski, and M. Walker, Phys. Rev. C **31**, 1550 (1985).
[38] H. Kudo, in *Workshop on Recoil Separator for Superheavy Element Chemistry*, Berkeley, CA, USA, 2003).
[39] C. E. Bemis, R. L. Ferguson, F. Plasil, R. J. Silva, F. Pleasonton, and R. L. Hahn, Phys. Rev. C **15**, 705 (1977).
[40] J. F. Wild, E. K. Hulet, R. W. Lougheed, K. J. Moody, B. B. Bandong, R. J. Dougan, and A. Veeck, J. Alloy. Comp. **213/214**, 86 (1994).
[41] A. N. Andreyev, D. D. Bogdanov, V. I. Chepigin, A. P. Kabachenko, O. N. Malyshev, R. N. Sagaidak, L. I. Salamatin, G. M. Terakopian, and A. V. Yeremin, Z. Phys. A **345**, 389 (1993).
[42] A. Türler, GSI Report No. 1989.
[43] Yu. Ts. Oganessian, V. K. Utyonkov, and K. J. Moody, Phys. Atom. Nucl. **64**, 1349 (2001).
[44] J. Dvorak *et al.*, Phys. Rev. Lett. **97**, 242501 (2006).
[45] J. Dvorak *et al.*, Phys. Rev. Lett. **100**, 132503 (2008).
[46] R. Smolańczuk, J. Skalski, and A. Sobiczewski, Phys. Rev. C **52**, 1871 (1995).
[47] R. Smolańczuk, Phys. Rev. C **56**, 812 (1997).
[48] I. Muntian, Z. Patyk, and A. Sobiczewski, Phys. Lett. B **500**, 241 (2001).
[49] W. Brüchle, Radiochim. Acta **91**, 71 (2003).
[50] H. Gäggeler *et al.*, Phys. Rev. C **33**, 1983 (1986).
[51] G. Guarino, A. Gobbi, K. D. Hildenbrand, W. F. J. Müller, A. Olmi, H. Sann, S. Bjørnholm, and G. Rudolf, Nucl. Phys. A **424**, 157 (1984).
[52] J. Tøke *et al.*, Nucl. Phys. A **440**, 327 (1985).

[53] Ch. E. Düllmann, C. M. Folden III, K. E. Gregorich, D. C. Hoffman, D. Leitner, G. K. Pang, R. Sudowe, P. M. Zielinski, and H. Nitsche, Nucl. Instrum. Methods A **551**, 528 (2005).
[54] K. Morita *et al.*, Eur. Phys. J. A **21**, 257 (2004).
[55] S. Hofmann *et al.*, Eur. Phys. J. A **10**, 5 (2001).
[56] S. Hofmann, Rep. Prog. Phys. **61**, 639 (1998).
[57] F. P. Heßberger *et al.*, Eur. Phys. J. A **41**, 145 (2009).
[58] I. Dragojević, K. E. Gregorich, Ch. E. Düllmann, J. Dvorak, P. A. Ellison, J. M. Gates, S. L. Nelson, L. Stavsetra, and H. Nitsche, Phys. Rev. C **79**, 011602(R) (2009).
[59] C. M. Folden III, K. E. Gregorich, Ch. E. Düllmann, H. Mahmud, G. K. Pang, J. M. Schwantes, R. Sudowe, P. M. Zielinski, H. Nitsche, and D. C. Hoffman, Phys. Rev. Lett. **93**, 212702 (2004).

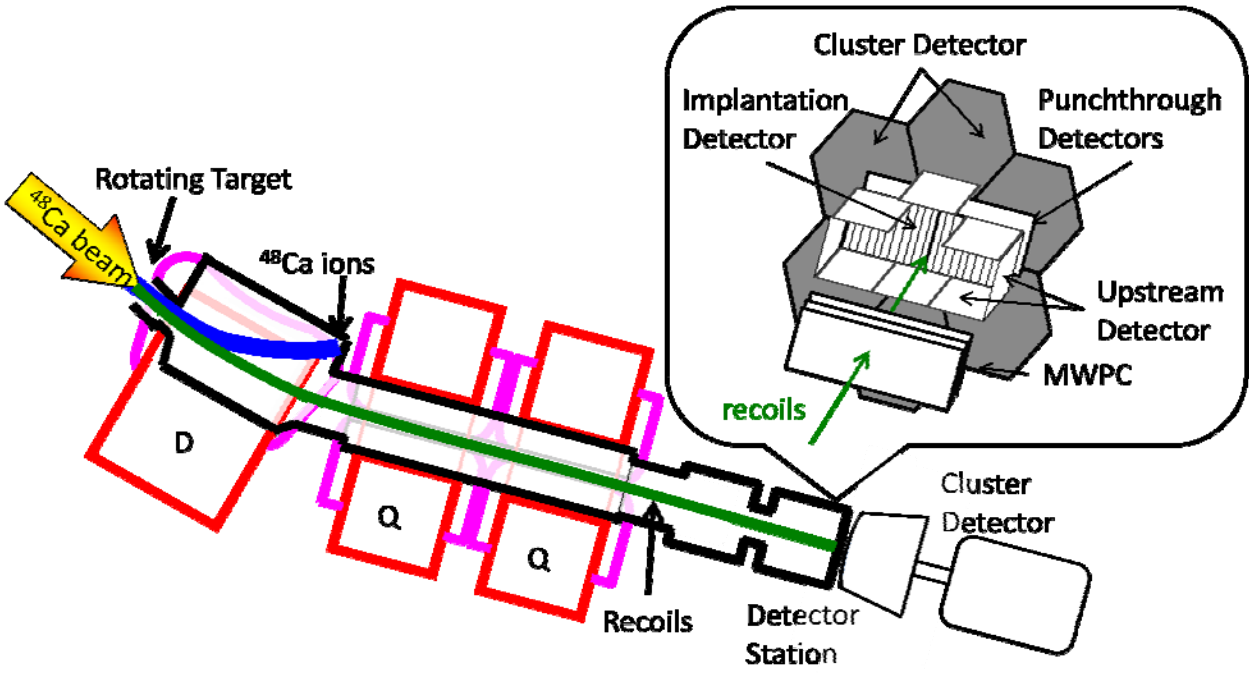

FIG. 1: (Color Online). Layout of TASCA and the detector setup. D is a dipole magnet and Q is a quadrupole magnet. The figure is not to scale.

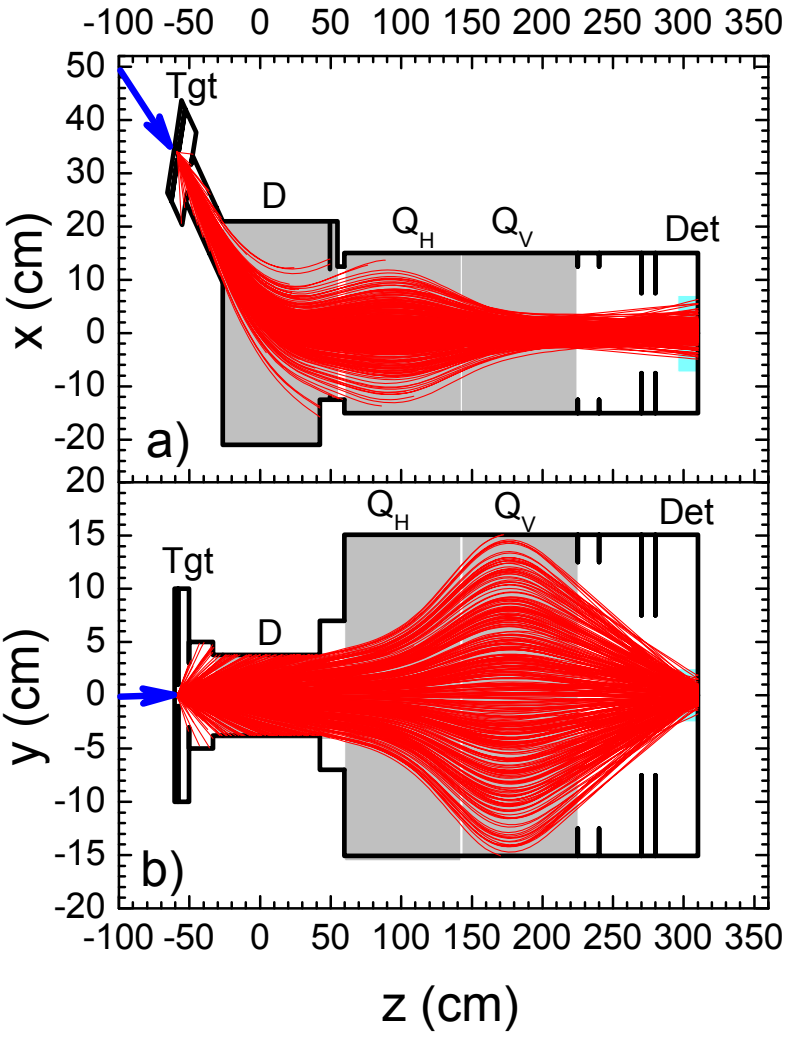

FIG. 2: (Color Online). Horizontal (a) and vertical (b) cross sectional views of expected element 114 EVR trajectories inside of TASCA for HTM. The thick line is a representation of the TASCA vacuum chambers inside the magnets where D is the dipole magnet and Q_H and Q_V are the horizontally and vertically focusing quadrupole magnets, respectively. Det and Tgt indicate the position of the detector and target, respectively. The labels on the axes are the distance (in cm) from the center of the dipole chamber in TASCA as defined in the Monte Carlo simulation. They are skewed to better show trajectories of individual particles. Beam enters TASCA from the left, passing through the center of the target area, as shown by the arrows. The predicted element 114 EVR trajectories are curved lines filling TASCA.

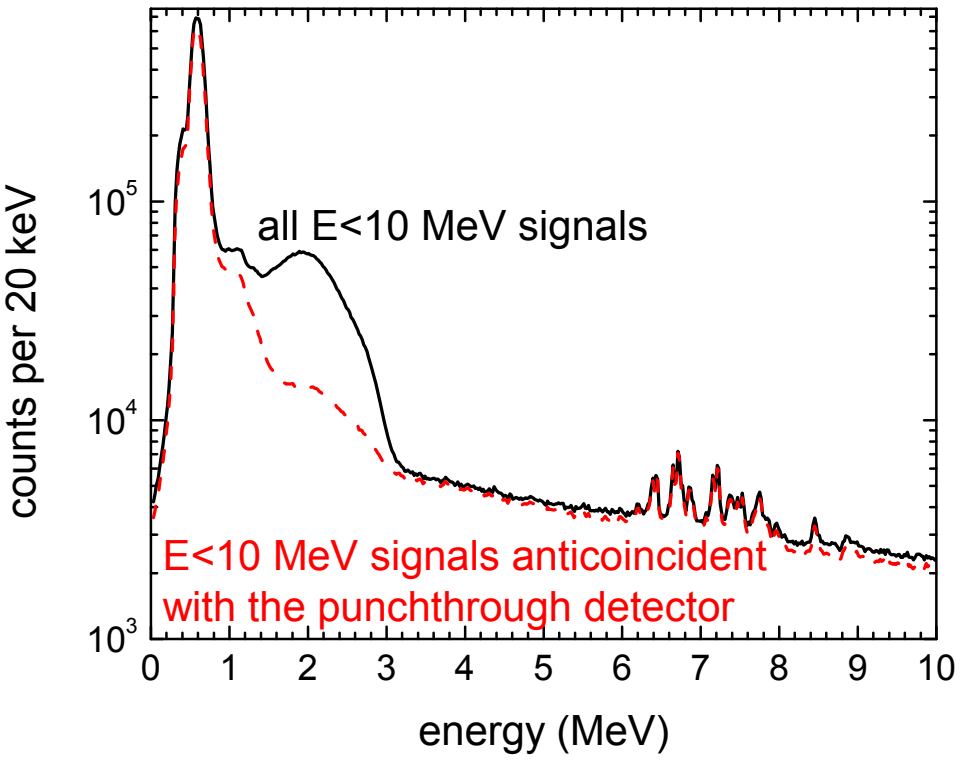

FIG. 3: (Color online) Spectra of all data with E<10 MeV from the 259.4-MeV HTM run (solid) and all data with E<10 MeV that was anticoincident with a signal from the punchthrough detector (dashed).

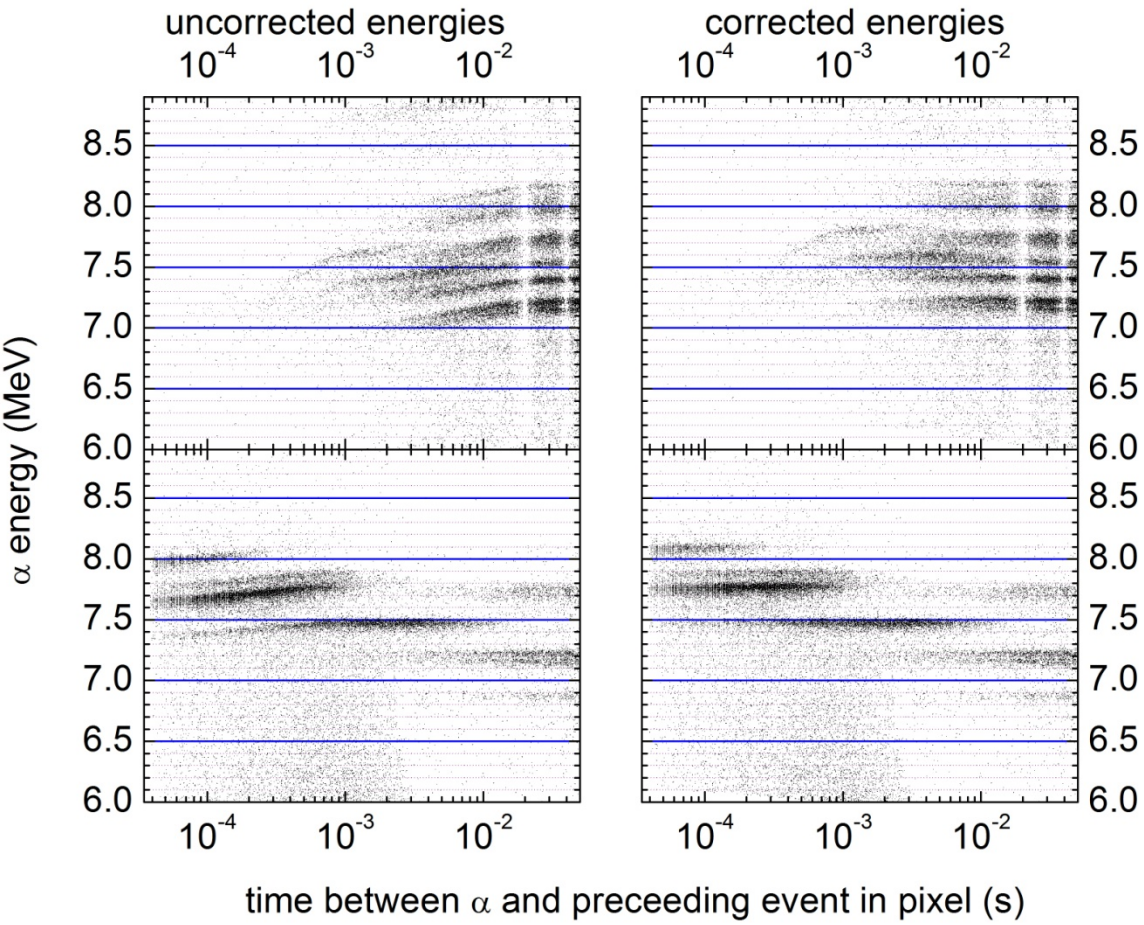

FIG. 4: (Color online) Uncorrected (left) and corrected (right) energies of α-particles from transfer reactions occurring in the same pixel and immediately following a high-energy EVR [$40<E_{EVR}(MeV)<60$] (top) or an α-particle [$6.0<E_{\alpha}(MeV)<9.0$] (bottom) within 0.05 s. The time structure in the top graphs is a result of requiring α-particles to occur outside of the beam pulse.

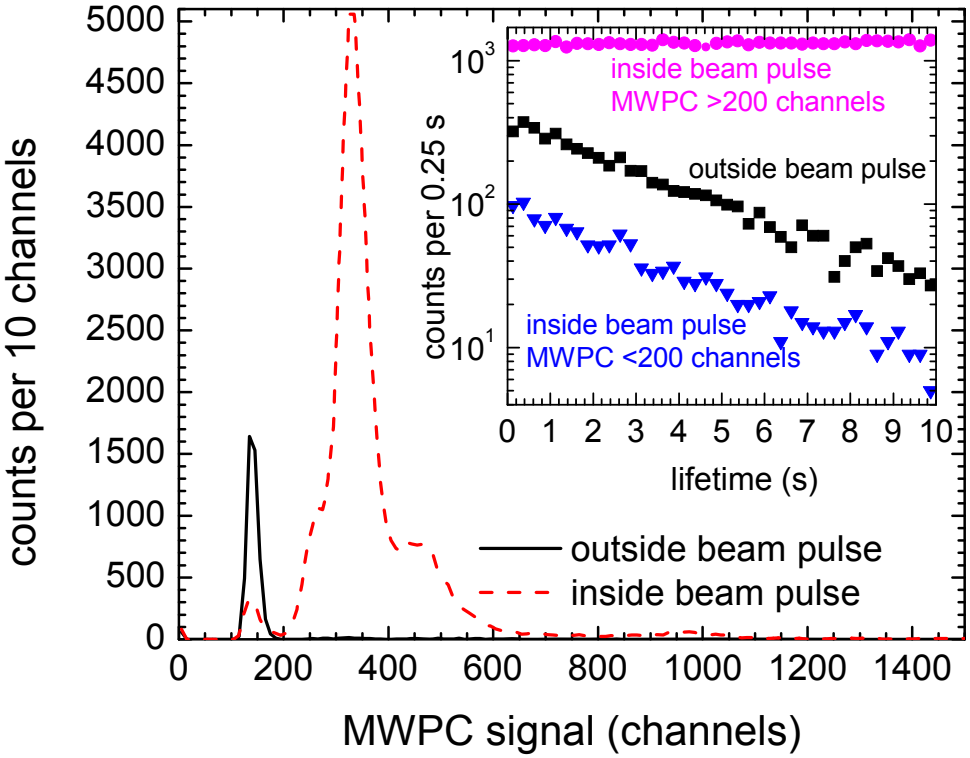

FIG. 5: (Color Online) Spectra of MWPC data from correlations between EVR-like and high-energy [80<E(MeV)<250] events during the ^{206}Pb(^{48}Ca,2n)^{252}No experiment with the high-energy event occurring either outside (solid) or inside (dashed) the beam pulse. The insert shows the time difference between each high-energy event and the associated EVR-like event for all correlations with the high-energy event occurring outside of the beam pulse (●), and for all correlations with the high-energy event occurring inside the beam pulse with MWPC signals either >200 channels (■) or <200 channels (▼).

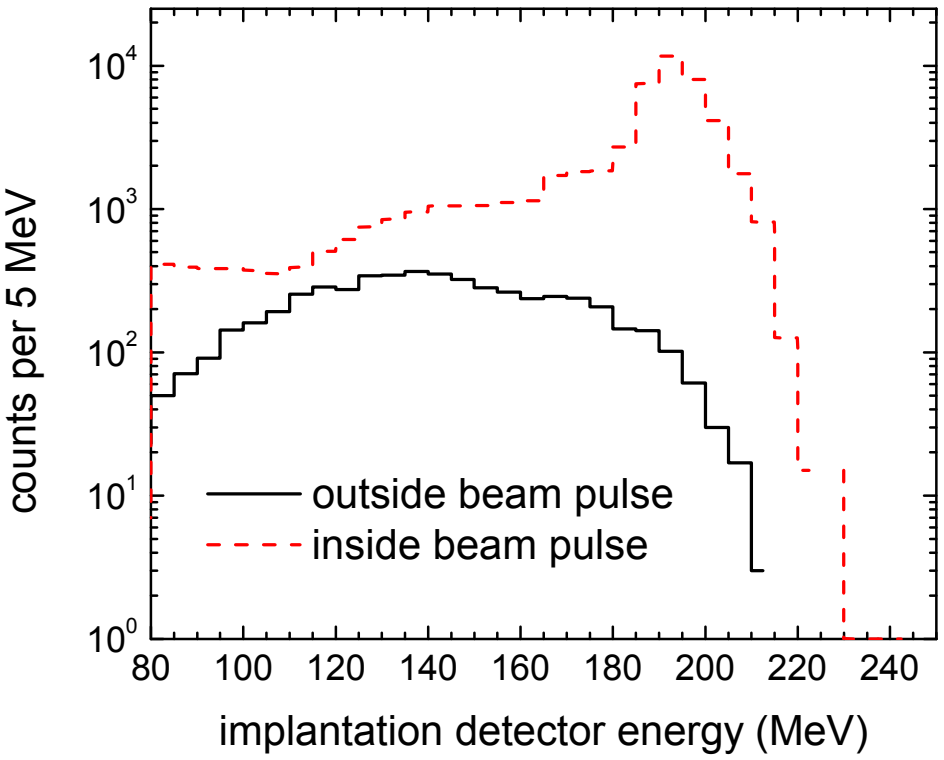

FIG. 6: (Color online) Energy spectra of all high-energy-events from correlations between EVR and high-energy [80<E(MeV)<250] events during the ^{206}Pb(^{48}Ca,2*n*)^{252}No experiment when the high-energy event occurring either outside (solid) or inside (dashed) the beam pulse.

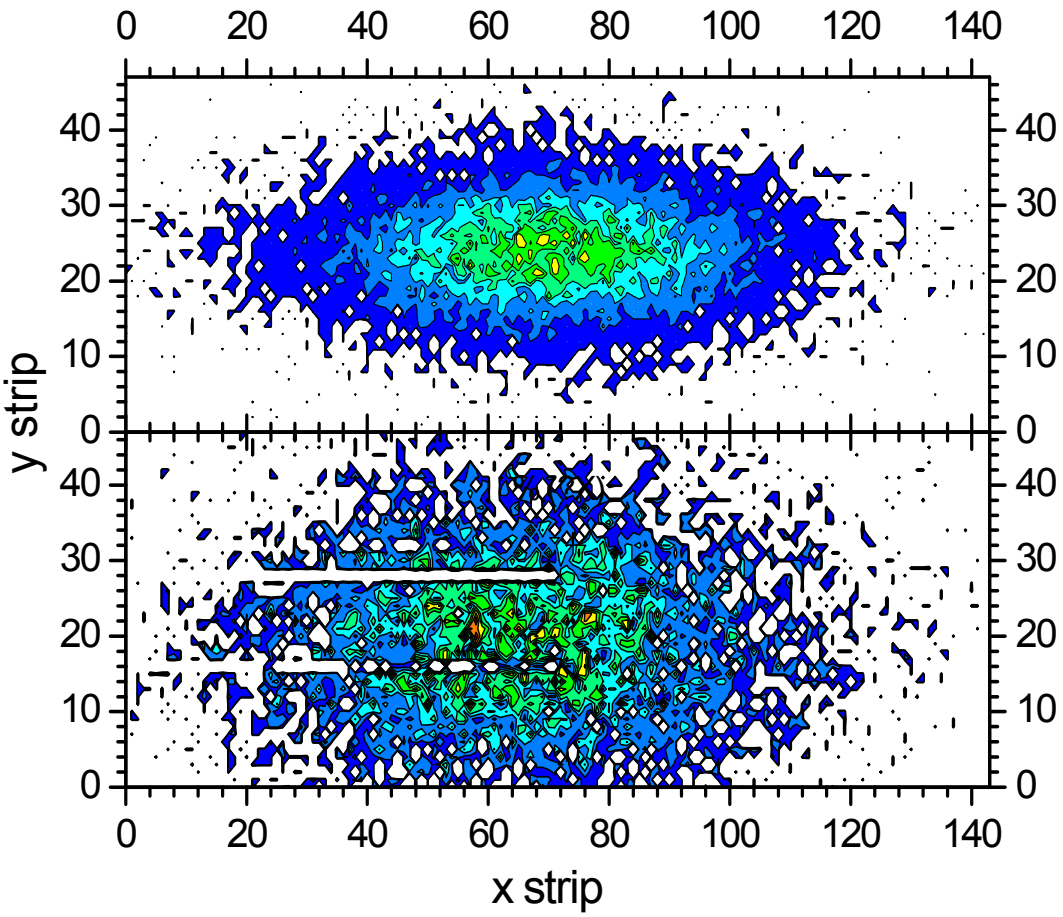

FIG. 7 (color online): Simulated (top) and experimental (bottom) distribution ^{252}No decays for the HTM of TASCA. Y-strips 16 and 28 were not working properly, as indicated by the lack of counts.

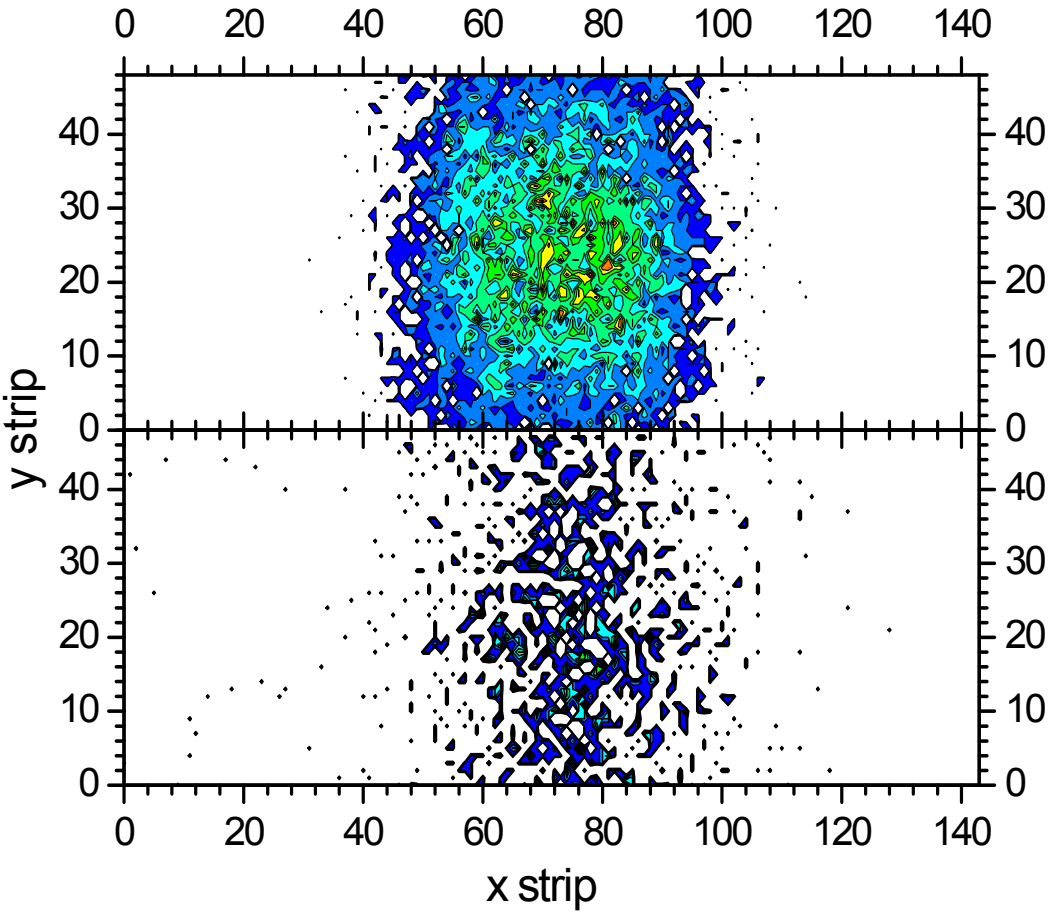

FIG. 8 (color online): Simulated (top) and experimental (bottom) distribution ^{254}No decays for the SIM of TASCA.

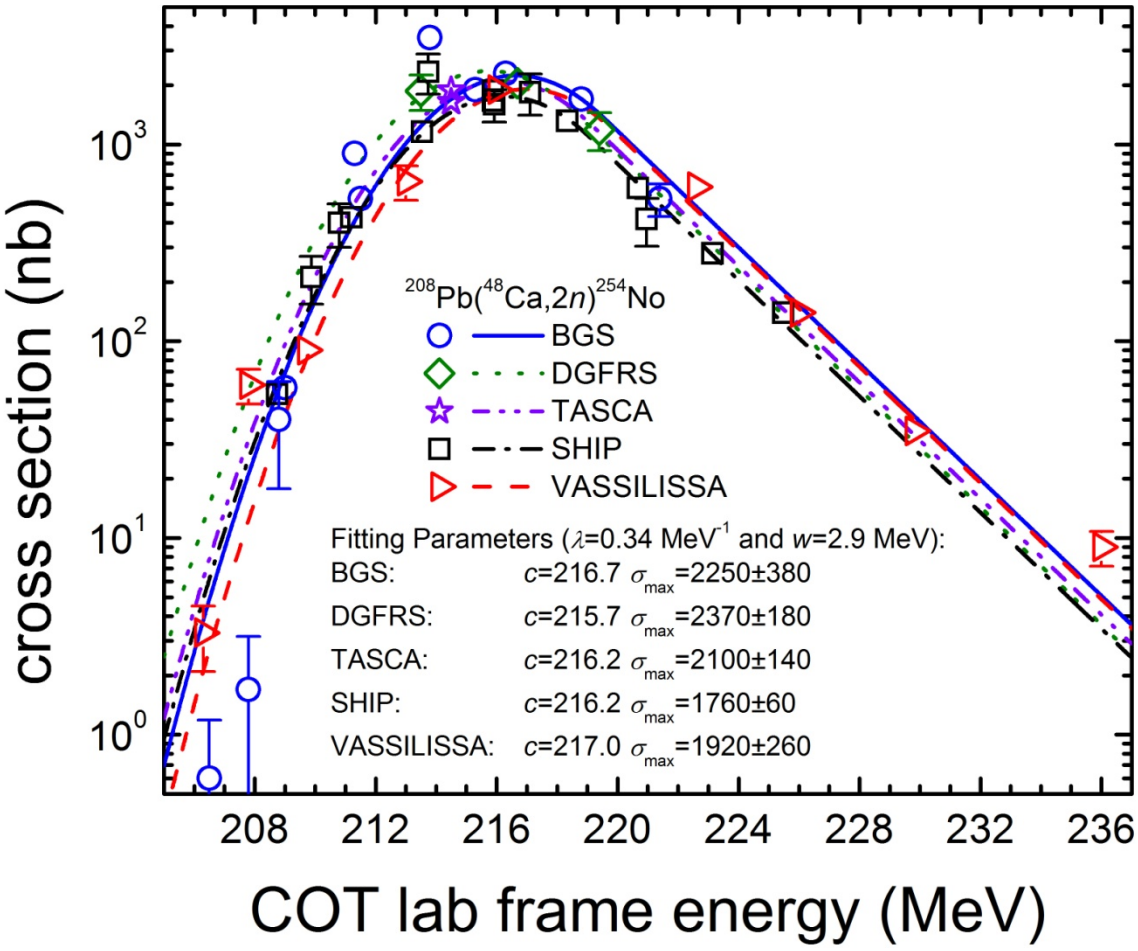

FIG. 9. (Color online) ^{208}Pb(^{48}Ca,2n)^{254}No excitation functions measured at the BGS (○), TASCA(☆), the DGFRS (◊), SHIP (□) and VASSILISSA (Δ). Error bars are shown when larger than the points and represent statistical errors only. The lines are fits to the excitation functions as described in Section III.C.2, with the λ=0.34 MeV^{-1} and w=2.9 MeV. c and σ were allowed to vary and converged to the values shown in the Figure.

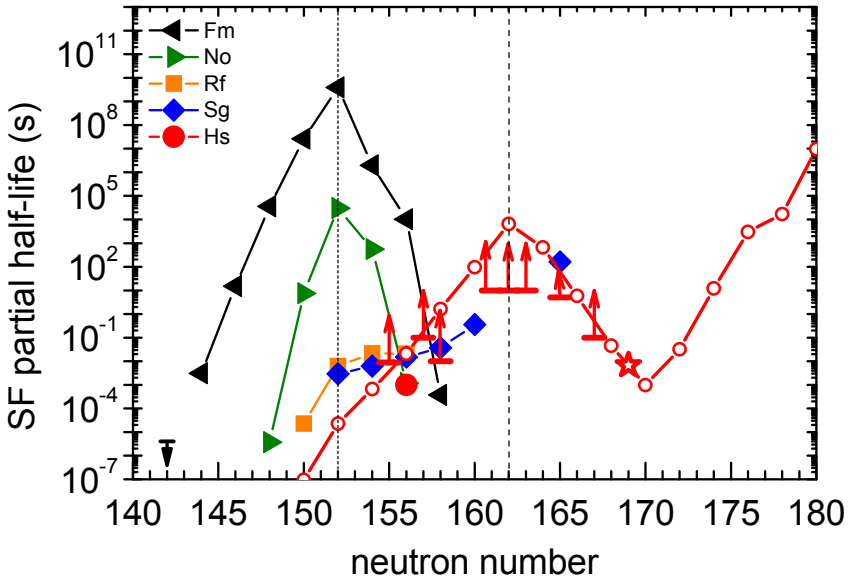

FIG. 10: (Color Online) Systematics of spontaneous fission partial half-lives *vs*. neutron number. Solid symbols show experimental data. Dashed lines: locations of deformed shell-closures at *N*=152, 162. Experimental data for Fm and No isotopes highlight the influence of the *N*=152 shell closure (solid triangles). The hassium isotopic chain covers the region around the *N*=162 shell. Open circles show calculated values for even Hs isotopes [46]. The experimental point for ^{264}Hs is shown by the solid circle. Experimental lower limits are shown with arrows. Our data point for ^{277}Hs is shown by the open star. The experimental [23, 44, 45, 54-59] Hs isotopic chain pattern show that the influence of the *N*=162 shell vanishes as the minimum between the "island of deformed superheavy nuclei" centered at ^{270}Hs and the predicted "island of spherical superheavy nuclei" near *N*=184 is approached.

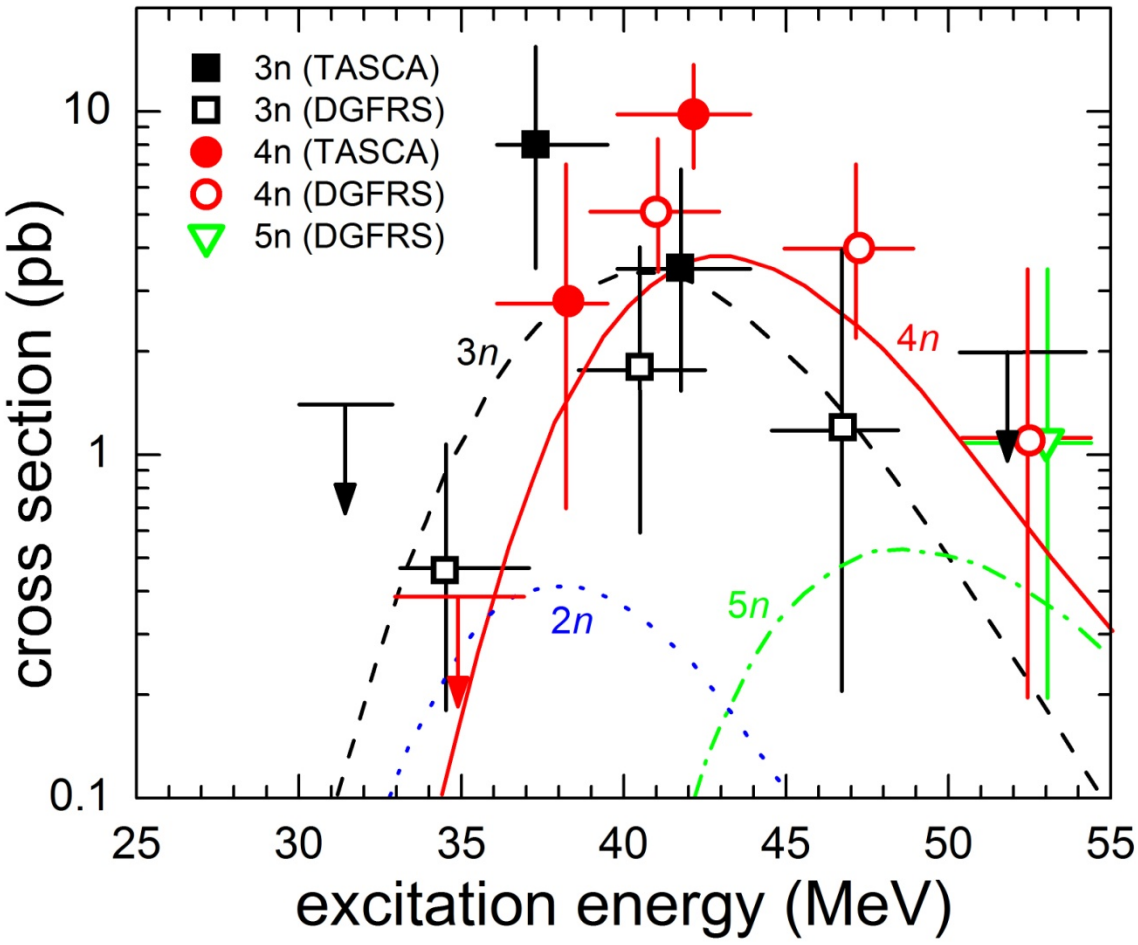

FIG. 11: (Color online) Cross sections for the ^{244}Pu(^{48}Ca,3-4*n*) reaction as observed in this work (solid symbols) and from [23] (open symbols). Lines are cross section predictions for the 2, 3, 4 and 5*n* exit channels from [22].

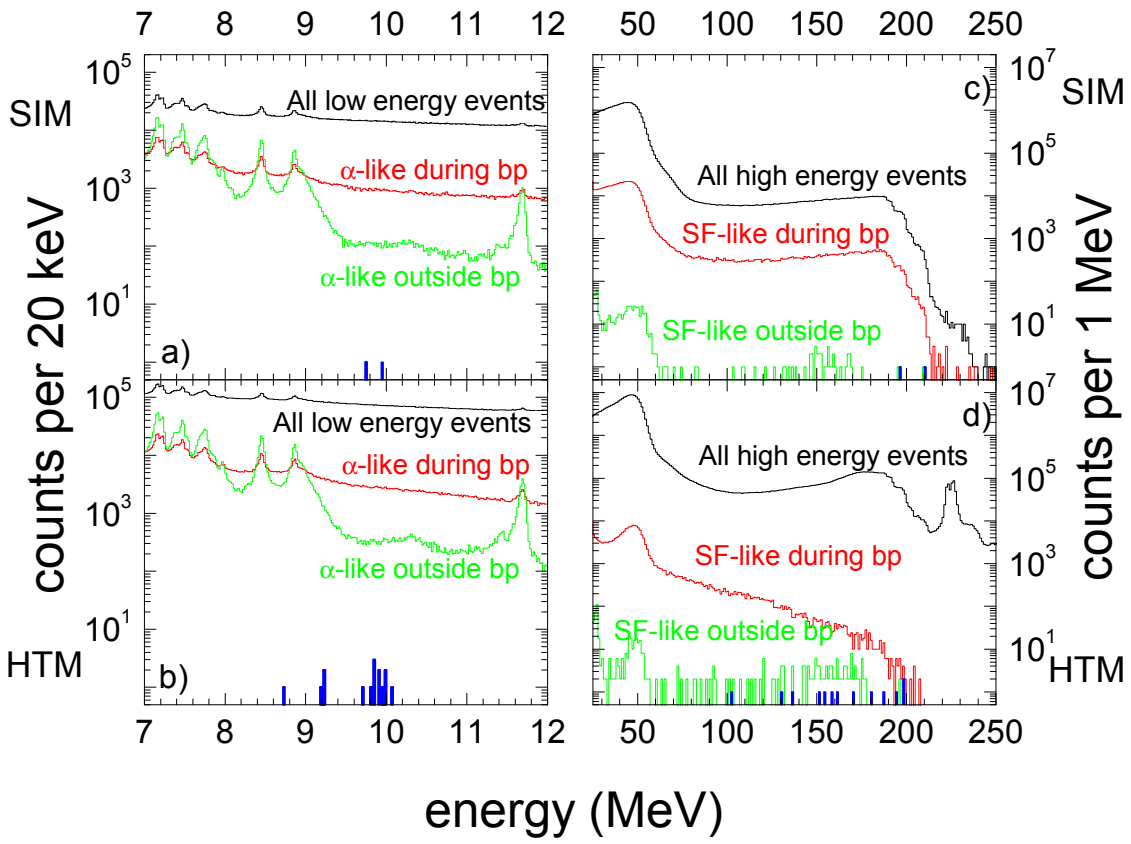

FIG. 12: (Color online) Energy spectra recorded in the ID during the 259.4-MeV HTM irradiation. (Left) Total energy spectra of all low energy events and α-like signals during the beam pulse (bp) and outside of the beam pulse for the SIM (a) and HTM (b) portions of the run. (Right) Total energy spectra of all high energy events and SF-like signals during and outside of the beam pulse for the SIM (c) and HTM (d) portions of the run. The blue histograms show the energies of α-events (in b) and ID portion of energies of the SF-events (in d) observed in correlated decay chains.

Table I: List of experiments with ^{48}Ca beams included in this paper.

Target	Exit channel	Product	E^* (MeV)	E_{beam} (MeV)	TASCA mode	$B\cdot\rho$ (T·m)	Beam dose ($\times 10^{16}$)	ε_{TASCA}[a] (%)	Cross section[a]	Cross section from Literature[b]
^{206}Pb	2*n*	^{252}No	21.2±2.0	231.2	HTM	2.10	10.0	56±6	(310±10) nb	SHIP: (430±10) nb [13] DGFRS: (500±40) nb [6]
^{206}Pb	2*n*	^{252}No	21.2±2.0	231.2	HTM	2.22	0.9			
^{206}Pb	2*n*	^{252}No	21.2±2.0	231.2	HTM	1.98	1.3			
^{207}Pb	2*n*	^{253}No	20.7±1.9	231.2	HTM	2.10	3.9	56±6	(760±10) nb	DGFRS: (1110±190)nb [6]
^{208}Pb	2*n*	^{254}No	20.5±1.9	231.2	HTM	2.10	1.4	56±6	(1890±40) nb	BGS: (2270±190) [8]
^{208}Pb	2*n*	^{254}No	20.5±1.9	231.2	SIM	2.10	1.3	40±4	(1650±40) nb	DGFRS: (2300±120) [6] SHIP: (1800±80) [12-14, 42] VASSILISSA: (1810±440) [15]
^{244}Pu	3*n*	^{289}114	$41.7^{+2.2}_{-1.9}$	259.4	HTM	2.23	244	60±6	$3.5^{+3.3}_{-2.0}$ pb	
^{244}Pu	3*n*	^{289}114	$37.5^{+2.0}_{-1.4}$	254.6	HTM	2.28	115	59±6	$8.0^{+7.4}_{-4.5}$ pb	DGFRS: $1.7^{+2.5}_{-1.1}$ pb
^{244}Pu	3*n*	^{289}114	$41.7^{+2.2}_{-1.9}$	259.4	SIM	2.28	100	35±4	<27 pb[c]	
^{244}Pu	4*n*	^{288}114	$41.7^{+2.2}_{-1.9}$	259.4	HTM	2.23	244	60±6	$9.8^{+3.9}_{-3.1}$ pb	
^{244}Pu	4*n*	^{288}114	$37.5^{+2.0}_{-1.4}$	254.6	HTM	2.28	115	59±6	$2.8^{+4.2}_{-2.1}$ pb	DGFRS: $5.3^{+3.6}_{-2.1}$ pb
^{244}Pu	4*n*	^{288}114	$41.7^{+2.2}_{-1.9}$	259.4	SIM	2.28	100	35±4	11^{+15}_{-7} pb	

[a] ε_{TASCA} and Cross sections were not calculated for ^{206}Pb(^{48}Ca,2*n*)^{252}No at B·ρ settings of 2.22 and 1.98 T·m as the products were not centered in the FPD.

[b] Cross sections for the $^{206\text{-}208}$Pb(^{48}Ca,2*n*)$^{252\text{-}254}$No reactions are reported at the maximum of a fit to available data as described in Section III.C.2.

[c] upper limit based on 95% confidence interval.

Table II: Search conditions for decay chains.

Isotope	Chain type	Number of chain member			
		1	2	3	4
^{252}No	α-only	α: 8.25<E_α(MeV)<8.55[b]			
	EVR-α	EVR: [5.0<E_{EVR}(MeV)<12.0][a]	α: 8.25<E$_\alpha$(MeV)<8.55[b] $\Delta t_{EVR\text{-}\alpha}$ < 6.9 s		
	EVR-α-α	EVR: [5.0<E_{EVR}(MeV)<12.0][a]	α: 8.25<E$_\alpha$(MeV)<8.55[b] $\Delta t_{EVR\text{-}\alpha}$ < 6.9 s	α: 7.7<E$_\alpha$(MeV)<7.95[b] $\Delta t_{\alpha\text{-}\alpha}$ < 108 s	
	EVR-SF	EVR: [5.0<E_{EVR}(MeV)<12.0][a]	SF: 80<E_{SF}(MeV)<300[b] E_{ID}<200 MeV $\Delta t_{EVR\text{-}SF}$ < 6.9 s		
^{253}No	α-only	α: 7.85<E_α(MeV)<8.25[b]			
^{254}No	α-only	α: 7.85<E_α(MeV)<8.25[b]			
^{288}114	EVR-α-SF	EVR: [3.0<E_{EVR}(MeV)<15.0][a]	α: 9.7<E$_\alpha$(MeV)<10.2 $\Delta t_{EVR\text{-}\alpha}$ < 7 s	SF: 80<E_{SF}(MeV)<300 E_{ID}<200 MeV $\Delta t_{\alpha\text{-}SF}$ < 1 s	
^{289}114	EVR-α-α-SF	EVR: [3.0<E_{EVR}(MeV)<15.0][a]	α: 9.7<E$_\alpha$(MeV)<10.2 $\Delta t_{EVR\text{-}\alpha}$ < 7 s	α: 9.0<E$_\alpha$(MeV)<9.5 $\Delta t_{\alpha\text{-}\alpha}$ < 150 s	SF: 80<E_{SF}(MeV)<300 E_{ID}<200 MeV $\Delta t_{\alpha\text{-}SF}$ < 50 s

[a] required to be inside of beam pulse with MWPC signal >200 channels

[b] required to be outside of the beam pulse with its full energy in the ID and MWPC signals <200 channels

Table III: Fitting parameters and maximum cross sections from fit to experimental data.

Reaction	Separator	global fit	best fit[b]				Reference
		σ_{max} (nb)[a]	λ (MeV^{-1})	c (MeV)	w (MeV)	σ_{max} (nb)[c]	
^{208}Pb(^{48}Ca,2n)^{254}No	BGS	2250±380	0.35	216	2.6	2270±190	[8]
	DGFRS	2370±180	0.34	216	**3.1**	2300±120	[6]
	TASCA	2000±140	**0.31**	**216**	**2.8**	2030±170	This work
	SHIP	1760±60	0.31	216	2.8	1800±80	[12, 14]
	VASSILISSA	1920±260	0.34	217	3.1	1810±440	[15]
^{207}Pb(^{48}Ca,2n)^{253}No	DGFRS	130±170	**0.34**	217	**2.6**	1190±130[d]	[6]
	TASCA	870±10	**0.31**	**216**	**2.8**	880±10	This work
^{206}Pb(^{48}Ca,2n)^{252}No	DGFRS	500±40	0.34	217	2.6	500±40	[6]
	TASCA	350±10	**0.31**	**216**	**2.8**	350±10	This work
	SHIP	430±10	**0.31**	216	**2.8**	430±10	[13]
	VASSILISSA	320±30	0.34	217	2.9	320±80	[15]

[a] Maximum cross sections as a result of a fit to experimental data with λ=0.34 MeV^{-1}, w=2.9 MeV. c and σ were allowed to vary.

[b] Numbers in **bold** were fixed for the fit, all other numbers were allowed to vary.

[c] Errors do not include systematic uncertainties.

[d] Increasing w to 3.1 MeV resulted in a similar σ_{max} = (1110±190) nb.

Table IV: Observed 114 decay chains in chronological order. For reconstructed energies, the energies recorded in the FPD and upstream detectors, respectively, are listed in parentheses. SF energies are shown in boldface.

E^* (MeV)	E_{beam} (MeV)	Chain no.	TASCA Mode	StopX Strip	StopY Strip	E_{EVR} (MeV)	Decay Energy (MeV)	Lifetime	^{A}Z	Prompt γ-rays[c]
41.7	259.4	1	HTM	22	11	6.41	9.847	3.589 s	$^{289}114$[a]	
							9.212	22.147 s	^{285}Cn[a]	
							8.727	5.688 s	^{281}Ds[a]	
							211 (136+75)	4.502 ms	^{277}Hs[a]	
41.7	259.4	2	HTM	91	18	6.51	9.982	0.242 s	$^{288}114$	0
							196(187+9)	0.130 s	^{284}Cn[a]	0
41.7	259.4	3	HTM	103	31	7.60	9.814 (1.236+8.578)	1.348 s	$^{288}114$[a]	0
							272 (130+142)	0.059 s	^{284}Cn[a]	1
41.7	259.4	4	HTM	83	18	5.97	10.062 (0.575+9.487)	0.649 s	$^{288}114$[a]	0
							163 (151+12)	0.171 s	^{284}Cn	0
41.7	259.4	5	HTM	102	24	8.69	9.915	0.446 s	$^{288}114$[a]	0
							194	0.087 s	^{284}Cn[a]	0
41.7	259.4	6	HTM	110	19+20[b]	7.99	9.919	1.164 s	$^{288}114$	0
							222 (158+64)	0.343 s	^{284}Cn[a]	1
41.7	259.4	7	HTM	119	29	9.10	9.980	0.242 s	$^{288}114$[a]	0
							180	0.026 s	^{284}Cn[a]	2
41.7	259.4	8	HTM	19	21+22[b]	13.22	9.947	0.763 s	$^{288}114$	0
							198	0.029 s	^{284}Cn[a]	1

41.7	259.4	9	HTM	86	20+21[b]	6.56	9.917	0.345 s	$^{289}114^{a}$	0
							9.194	51.037 s	$^{285}Cn^{a}$	0
							198	35.476 s	$^{281}Ds^{a}$	1
41.7	259.4	10	HTM	131	26	7.35	9.700 (0.838+8.862)	0.823 s	$^{288}114^{a}$	0
							170	0.063 s	$^{284}Cn^{a}$	1
37.5	254.6	11	HTM	89	24	8.67	9.965	0.482 s	$^{288}114^{a}$	0
							161	0.401 s	$^{284}Cn^{a}$	1
37.5	254.6	12	HTM	100	5	6.93	9.847	0.774 s	$^{289}114^{a}$	0
							9.229	9.542 s	$^{285}Cn^{a}$	0
							278 (154+124)	28.413 s	$^{281}Ds^{a}$	2
37.5	254.6	13	HTM	122	40	3.26	9.847	0.904 s	$^{289}114$	0
							9.220	92.202 s	$^{285}Cn^{a}$	0
							146 (102+44)	46.283 s	$^{281}Ds^{a}$	1[d]
41.7	259.4	14	SIM	59	47	8.458	9947	1.132 s	$^{288}114^{a}$	0
							210	0.043 s	$^{284}Cn^{a}$	2[d]
41.7	259.4	15	SIM	89	0	7.605	9848	0.921 s	$^{288}114$	0
							196	0.390 s	$^{284}Cn^{a}$	1

[a] Decay observed outside of beam pulses.

[b] All events in chain were split between two StopY strips

[c] Number of prompt γ-rays observed with each event. The detection of prompt γ-rays was not working for chain 1 (see Sec. III.D).

[d] Includes an add-back event of neighboring germanium crystals

Table V: Average rate of events over the ID during the HTM and SIM runs when target integrity was not compromised. The DC rate of events can be found by 0.25*(During beam pulse) + 0.75*(Outside of beam pulse).

Target	Event Type	During Beam pulse		Outside of Beam pulse	
		HTM	SIM	HTM	SIM
^{206}Pb	EVR: 3.0<E_{EVR}(MeV)<15.0	120 s^{-1}			
	α: 8.25<E_α(MeV)<8.55	0.37 s^{-1}		0.12 s^{-1}	
	α: 7.7<E_α(MeV)<7.95	0.33 s^{-1}		0.09 s^{-1}	
	α: 8.0<E_α(MeV)<12.0	3.13 s^{-1}		0.19 s^{-1}	
	SF: 80<E_{SF}(MeV)<300 E_{ID}(MeV)<200	0.08 s^{-1}		0.09 s^{-1}	
	All events	1800 s^{-1}		35 s^{-1}	
^{207}Pb	α: 7.85<E_α(MeV)<8.25	0.70 s^{-1}		0.43 s^{-1}	
	α: 8.0<E_α(MeV)<12.0	2.85 s^{-1}		0.39 s^{-1}	
	All events	1400 s^{-1}		32 s^{-1}	
^{208}Pb	α: 7.85<E_α(MeV)<8.25	1.44 s^{-1}	0.58 s^{-1}	1.04 s^{-1}	0.20 s^{-1}
	α: 8.0<E_α(MeV)<12.0	5.06 s^{-1}	1.76 s^{-1}	1.09 s^{-1}	0.50 s^{-1}
	All events	1700 s^{-1}	990 s^{-1}	43 s^{-1}	52 s^{-1}
^{244}Pu	EVR: 3.0<E_{EVR}(MeV)<15.0	206 s^{-1}	91 s^{-1}		
	α: 9.7<E_α(MeV)<10.2	1.13 s^{-1}	0.52 s^{-1}	0.05 s^{-1}	0.02 s^{-1}
	α: 9.0<E_α(MeV)<9.5	1.40 s^{-1}	0.71 s^{-1}	0.15 s^{-1}	0.07 s^{-1}
	α: 8.0<E_α(MeV)<12.0	10.33 s^{-1}	0.53 s^{-1}	1.21 s^{-1}	0.61 s^{-1}
	SF: 80<E_{SF}(MeV)<400 E_{ID}(MeV)<200	0.04 s^{-1}	0.44 s^{-1}	3.31E-4 s^{-1}	8.88E-5 s^{-1}
	All events	2900 s^{-1}	2084 s^{-1}	670 s^{-1}	640 s^{-1}